

ORIGINAL ARTICLE

Haploinsufficiency of the 22q11.2 microdeletion gene *Mrpl40* disrupts short-term synaptic plasticity and working memory through dysregulation of mitochondrial calcium

P Devaraju¹, J Yu¹, D Eddins¹, MM Mellado-Lagarde¹, LR Earls^{1,3}, JJ Westmoreland^{1,3}, G Quarato², DR Green² and SS Zakharenko¹

Hemizygous deletion of a 1.5- to 3-megabase region on chromosome 22 causes 22q11.2 deletion syndrome (22q11DS), which constitutes one of the strongest genetic risks for schizophrenia. Mouse models of 22q11DS have abnormal short-term synaptic plasticity that contributes to working-memory deficiencies similar to those in schizophrenia. We screened mutant mice carrying hemizygous deletions of 22q11DS genes and identified haploinsufficiency of *Mrpl40* (mitochondrial large ribosomal subunit protein 40) as a contributor to abnormal short-term potentiation (STP), a major form of short-term synaptic plasticity. Two-photon imaging of the genetically encoded fluorescent calcium indicator GCaMP6, expressed in presynaptic cytosol or mitochondria, showed that *Mrpl40* haploinsufficiency deregulates STP via impaired calcium extrusion from the mitochondrial matrix through the mitochondrial permeability transition pore. This led to abnormally high cytosolic calcium transients in presynaptic terminals and deficient working memory but did not affect long-term spatial memory. Thus, we propose that mitochondrial calcium deregulation is a novel pathogenic mechanism of cognitive deficiencies in schizophrenia.

Molecular Psychiatry (2017) **22**, 1313–1326; doi:10.1038/mp.2016.75; published online 17 May 2016

INTRODUCTION

Schizophrenia (SCZ) is a catastrophic disease that affects approximately 1% of the world's population and is characterized by multiple symptoms that include cognitive abnormalities such as deficits in working memory, executive function and learning.¹ Mechanisms of cognitive symptoms of SCZ are poorly understood, partly because only weak associations have been identified between any single gene and the disease, and valid animal models have been lacking.² Mouse models of 22q11.2 deletion syndrome (22q11DS) are among the few animal models that replicate abnormalities associated with SCZ. The 22q11DS is the most common multigene syndrome in humans and is considered a genetic risk factor for SCZ. The 22q11DS is caused by the hemizygous deletion of a 1.5- to 3-megabase region on the q arm of chromosome 22, resulting in the haploinsufficiency of multiple genes.³ Approximately 30% of children with 22q11DS experience SCZ during late adolescence or early adulthood.^{4,5} Symptoms of 22q11DS-related SCZ are indistinguishable from those of the idiopathic disease,⁵ suggesting that the biological mechanisms involved in SCZ arising from the 22q11 deletion are similar to those involved in non-deletion-related SCZ.

The diagnosis of SCZ usually includes positive symptoms (i.e., disorderly thinking, hallucinations and delusional ideas), negative symptoms (i.e., low levels of emotional arousal or social activity) and cognitive symptoms (i.e., deficits in attention, working memory, executive function, and learning and memory). Recognition of cognitive deficits as a core feature of SCZ and 22q11DS is increasing, as these deficits better predict disease progression than do the other symptoms.^{6,7} Many cognitive symptoms of SCZ are thought to originate in the hippocampus,^{8,9} a key brain region

involved in learning and memory. Spatial working-memory deficits occur in patients with 22q11DS^{10,11} and are also seen in 22q11DS mouse models. Mouse models of 22q11DS exhibit abnormal hippocampal short- and long-term synaptic plasticity,^{12,13} which is consistent with the notion that synaptic plasticity is a cellular mechanism of learning and memory.¹⁴ Short-term synaptic plasticity in the form of short-term potentiation (STP) acting on the millisecond-to-minute time scale is believed to underlie reliable information transfer between hippocampal excitatory synapses in an activity-dependent manner,^{14–17} working memory¹⁸ and decision making.¹⁹ STP predominantly occurs in presynaptic neurons.²⁰ Several studies have shown that presynaptic abnormalities can be attributed to dysregulation of presynaptic calcium (Ca²⁺). For example, altered STP resulting from deregulated presynaptic Ca²⁺ is seen in models of neuropsychiatric diseases such as FMRP-related autism, Alzheimer disease and 22q11DS.^{12,21,22} Because 22q11DS is a multigene deletion syndrome, more than one gene may affect STP. Initially, STP dysregulation in *Df(16)1^{+/-}* models of 22q11DS was linked to haploinsufficiency of the microRNA-processing gene *Dgcr8*,²³ which is mapped to a proximal part of the microdeletion. Depletion of microRNAs *miR-185* and *miR-25* leads to presynaptic Ca²⁺ dysregulation and abnormal STP through the abnormal elevation of (sacro)endoplasmic reticulum ATPase type 2 (Serca2), the Ca²⁺ pump that extrudes Ca²⁺ from the cytoplasm into the endoplasmic reticulum.²³ SERCA2 is also elevated in the hippocampus of schizophrenic patients,²³ and the most comprehensive genome-wide association study to date linked the *ATP2A2* gene, which encodes SERCA2, with SCZ.²⁴ Other genes that affect STP remain unknown.

¹Department of Developmental Neurobiology, St. Jude Children's Research Hospital, Memphis, TN, USA and ²Department of Immunology, St. Jude Children's Research Hospital, Memphis, TN, USA. Correspondence: Dr SS Zakharenko, Department of Developmental Neurobiology, St. Jude Children's Research Hospital, Mail Stop 323, Memphis, TN 38105, USA. E-mail: stanislav.zakharenko@stjude.org

³Current address: Department of Cell and Molecular Biology, Tulane University, New Orleans, LA 70118, USA.

Received 2 December 2015; revised 3 March 2016; accepted 17 March 2016; published online 17 May 2016

Here we report results of our STP screening of the distal region of the 22q11DS microdeletion, which encompasses six genes: *Cldn5*, *Cdc45l*, *Ufd1l*, *2510002D24Rik*, *Mrpl40* and *Hira*. Using mutant mice carrying hemizygous deletions of individual genes, we discovered that haploinsufficiency of *Mrpl40* (mitochondrial large ribosomal subunit protein 40, also known as *Nlvcf*) causes abnormal STP and short-term memory deficits via Serca2-independent deregulation of presynaptic Ca^{2+} . Using two-photon Ca^{2+} imaging of the genetically encoded Ca^{2+} indicator GCaMP6,²⁵ expressed either in the presynaptic cytosol or in mitochondria, we showed that *Mrpl40* haploinsufficiency hindered the extrusion of Ca^{2+} from the mitochondrial matrix through an impaired mitochondrial permeability transition pore (mPTP). This leads to abnormally high levels of Ca^{2+} in the presynaptic cytosol and elevated STP. Our data implicate *Mrpl40* as a 22q11DS gene, the haploinsufficiency of which contributes to cognitive deficits in microdeletion-related SCZ.

MATERIALS AND METHODS

Animals

Mature (16–20 weeks) mice of both sexes were used. Production and genotyping of *Df(16)5^{+/-}*, *Dgcr8^{+/-}*, *Cldn5^{+/-}* and *Hira^{+/-}* mice were previously described.^{23,26–28} To generate *Cdc45^{+/-}* and *Ufd11^{+/-}* mice, we obtained SIGTR embryonic stem (ES) cell clones containing gene-trap disruptions of the pGT01Lxr vector for *Cdc45l* (cell line AJ0425) and a *Ufd1l* allele (cell line AW0532) from the Mutant Mouse Regional Resource Center (University of California, Davis, CA, USA). The AJ0425 ES cell line carries a Genetrap insertion in exon 3 of the *Cdc45l* gene. Offspring were genotyped using the following primers: *Cdc45l*F: GCTGGGTACCTGAGTGTCATTG, *Cdc45l*R: CGAGACTGGTATGTGTGTGTGTG, and the betageo primer 2: ATTCAGGCTGCGCAACTGTTGGG, producing a 353-bp wild-type (WT) amplicon and a 309-bp mutant amplicon. The AW0532 ES cell line disrupts the *Ufd1l* gene in the first intron. This line was genotyped with the following primers: *Ufd1l*F: GTTGACGCTAACGTCAGTCAC, *Ufd1l*R: GAAGCAGC GGTACTGCGTGGAG, and the Betageo primer: ATTCAGGCTGCGCAACT GTTGG, producing a 612-bp WT amplicon and a 304-bp mutant amplicon.

To generate the *Mrpl40^{+/-}* mice, we obtained sperm from the C57BL/6 strain carrying the *Mrpl40^{tm1(KOMP)vicg}* allele of the *Mrpl40* gene from the trans-NIH Knock-Out Mouse Project (www.komp.org). Sperm was used to produce *Mrpl40^{+/-}* offspring via *in vitro* fertilization. *Mrpl40^{+/-}* mice were genotyped using the following primers: *Mrpl40*F: CAGGCACACGTCAGACA CA, *Mrpl40*R: GAGATCCCAGAAGGCCAGTAAG, and LacZR: CCCACCAGAG AGCTTC, producing a 102-bp WT amplicon and a 387-bp mutant amplicon. To expand the colony, we bred *2510002D24Rik^{+/-}*, *Mrpl40^{+/-}*, *Ufd11^{+/-}* and *Cdc45^{+/-}* mice harboring the disrupted alleles to C57BL/6 J mice in the St. Jude Children's Research Hospital (St. Jude) Animal Resource Center.

All mouse strains in this study were back-crossed onto the C57BL/6 J genetic background for at least five generations. Individual experiments were conducted in age-matched and sex-matched animals. The care and use of animals were reviewed and approved by the Institutional Animal Care and Use Committee at St. Jude.

Brain slice preparation

Mouse brains were quickly removed and placed in cold (4 °C) dissecting artificial cerebrospinal fluid (ACSF) containing 125 mM choline-Cl, 2.5 mM KCl, 0.4 mM $CaCl_2$, 6 mM $MgCl_2$, 1.25 mM NaH_2PO_4 , 26 mM $NaHCO_3$ and 20 mM glucose (295–300 mOsm), under 95% O_2 /5% CO_2 , and acute transverse hippocampal slices (400- μ m-thick) were prepared. After dissection, slices were incubated for 1 h in ACSF containing 124 mM NaCl, 2.5 mM KCl, 2 mM $CaCl_2$, 2 mM $MgCl_2$, 1.25 mM NaH_2PO_4 , 26 mM $NaHCO_3$ and 10 mM glucose (285–295 mOsm), under 95% O_2 /5% CO_2 at 32–34 °C and then transferred into the submerged recording chamber and superfused (1.5–2 ml min^{-1}) with ACSF. Long-term potentiation experiments were performed as previously described.¹² Because the bath temperature is crucial for STP experiments,²⁹ all electrophysiology and imaging experiments were conducted in a perfusion chamber maintained at near physiological temperature (33–34 °C, measured at the center of the bath) by using both inline and bath heaters.

Whole-cell electrophysiology

Electrophysiological data were acquired using a Multiclamp 700B amplifier (Molecular Devices, Sunnyvale, CA, USA), filtered at 2 kHz and digitized at 10/20 kHz using a Digidata 1440 digitizer (Molecular Devices) controlled by Clampex acquisition software (Molecular Devices). All offline analyses of electrophysiological data were done in Clampfit. To evoke excitatory postsynaptic currents (EPSCs) in CA1 neurons, we stimulated Schaffer collaterals with a concentric bipolar stimulating electrode (125 μ m outer diameter; 12.5 μ m inner diameter) connected to a Master 8 stimulator and an Iso-Flex stimulus isolator (both A.M.P.I., Jerusalem, Israel) with 100- μ s pulses. Stimulating and recording electrodes were separated by at least 350–400 μ m. For STP experiments, a cut was placed between the CA3 and CA1 regions to avoid recurrent stimulation. Recording electrodes were borosilicate glass capillaries pulled in a P-1000 puller (Sutter Instruments, Novato, CA, USA) and had resistances approximately 3.5–5 M Ω . CA1 neurons were whole-cell voltage-clamped using electrodes filled with 130 mM K gluconate, 10 mM KCl, 0.5 mM EGTA, 2 mM $MgCl_2$, 5 mM NaCl, 2 mM ATP- Na_2 , 0.4 mM GTP- Na , 10 mM HEPES and 10–25 μ M Alexa 594 (pH 7.35, ~290 mOsm). EPSCs were recorded by holding the cells at –74 mV (accounting for a liquid junction potential of ~14 mV). Access resistance was monitored using a –5 mV step before each recording (range, 25–50 m Ω), and cells that displayed unstable access resistance (variations >20%) were excluded from the analyses. All EPSC recordings for STP experiments were done in the presence of the GABA_AR antagonist picrotoxin (100 μ M) to prevent inhibitory responses and the NMDA receptor antagonist D-2-amino-5-phosphonovalerate (D-AP5, 50 μ M) to avoid induction of long-term synaptic plasticity.

STP components were separated using an adapted procedure.²⁹ A baseline of stable EPSCs was established to evoke 150- to 200-pA EPSCs. Stimulation intensities ranged from 30 to 60 μ A and were held constant for each cell throughout the experiment. Stimulation intensity did not differ significantly between slices from WT and mutant littermates ($P > 0.05$). The stimulation protocol consisted of the following: 5 pre-train pulses (0.2 Hz), a high-frequency train (100 pulses, 80-Hz), 24 pulses at 5 Hz (to measure recovery from depression) and 24 pulses at 0.2 Hz (to measure augmentation). The 80-Hz (100 pulses) train was chosen because it induced both strong depression and augmentation on the basis of STP induced by trains of different frequencies (data not shown). EPSCs during and after the train were normalized to the average of the five pre-train EPSCs (shown as a single baseline point), and the amplitudes are reported as normalized EPSC peak amplitudes. For each cell, we averaged the data from 3 to 4 trials by using this stimulation protocol. To measure the EPSC amplitudes during the train, we resorted to a binning procedure, instead of the template waveform-based subtraction protocol, as previously described.²⁹ The measured EPSC train of 1250 ms (80 Hz \times 100 pulses) was divided into 100 equal bins of 12.5 ms, and the peak amplitude within each bin was graphed as the normalized EPSC amplitude during the train. This procedure was sufficient to separate EPSCs in the train.

Augmentation, the slowest component of STP, has negligible contamination from depression and facilitation and is reported as measured without corrections. Statistical comparisons of augmentation were made using the measured peak augmentation at 5 s after the 80-Hz train, instead of the extrapolated augmentation at 0 s. Recovery from depression (200–4800 ms) after the 80-Hz train was contaminated by augmentation and some residual facilitation. Because the EPSCs measured during the recovery phase had an interstimulus interval of 200 ms, the contamination by facilitation was minimal and corrected only for overlying augmentation. To that end, the measured augmentation decay curve (5–120 s after the 80-Hz train) was extrapolated from 200 to 4800 ms after the train by using a standard exponential fit in Clampfit. The normalized EPSCs during the recovery phase were then corrected for the overlying extrapolated augmentation for each time point. Facilitation was measured in separate experiments by using paired pulses at interstimulus intervals of 20–1000 ms.

To measure excitability, we held CA3 neurons in current clamp mode and added D-AP5 (50 μ M) and picrotoxin (100 μ M) to the external ACSF bath to avoid possible long-term effects. Action potential (AP) parameters were estimated by clamping the cell at –65 mV using automatic slow-current injection. Input resistance, AP threshold, rheobase (intensity of current reached at threshold) and number of APs (evoked by holding at the minimum current needed to reach threshold) were measured by injecting 1-s steps of 25-pA current (12 steps from –25 pA to 250 pA). To measure AP widths, we evoked APs by injecting five short current steps (1500–2000 pA, 1-ms duration, 0.2 Hz). AP durations were calculated as the

time interval between the up-stroke and down-stroke of the AP waveform at -10 mV. AP duration during the 80-Hz train was normalized to the AP duration at baseline, as previously described.²¹ Electrophysiology experiments were done without blinding.

Generation of plasmids and viruses

To generate adeno-associated viruses (AAVs) expressing cytoplasmic GCaMP6f (GCaMP6) and mitochondrial-targeted GCaMP6f (mitoGCaMP6), we used PCR to amplify the human synapsin promoter (hSyn) from pAAV-6P-SEWB.³⁰ The pAAV-GFP (Addgene plasmid 32395) was cut with *Sna*B1 and *Sac*1 to replace CMV with hsyn (pAAV-hsyn-GFP). *Eco*RI and *Bam*HI were used to replace GFP with mCherry to generate pAAV-hsyn-mCherry. To generate pAAV-hSyn-mCherry-2A-GCaMP6, oligonucleotides containing the coding sequence for the 2A peptide were used for PCR amplification of GCaMP6 from pGP-CMV-GCaMP6 (Addgene plasmid 40755). To generate pAAV-hSyn-mCherry-2A-mitoGCaMP6, oligonucleotides containing the coding sequence for the 2A peptide and the mitochondrial-targeting sequence (MSVLTPLLLRGLTGSARRLPVPRAKIHS) were used for PCR amplification of GCaMP6 from pGP-CMV-GCaMP6 (Addgene plasmid 40755). To generate AAV-*Slc25a4* OE, we used PCR to amplify the open reading frame of *Slc25a4*. *Drd2* open reading frame from AAV-CamKIIa-*Drd2* OE³¹ was replaced with the *Slc25a4* open reading frame using *Hind*III. DNA sequencing was used to verify the absence of PCR-induced mutations. Lentivirus vector siRNA plasmids (control shRNA, 5'-TACGTCCAAGGTCGGGCAGGAAGA-3'; *Slc25a4* shRNA1, 5'-GCAAGGGATC TTCCCAGCGAGAATCAAT-3'; *Slc25a4* shRNA2, 5'-CGTTTGACACTGTTCTCGTAGGATGATG-3'; *Slc25a4* shRNA3, 5'-GCACATTATCGTGAGCTGGATGATT GCCC-3') were generated by Applied Biological Materials (Richmond, BC, Canada). Viruses (1.8×10^8 to 1×10^9 particles ml^{-1}) were produced by either the St. Jude or University of Tennessee Health Sciences Center Viral Vector Cores.

Two-photon imaging of presynaptic calcium and *in vivo* injections

Two-photon laser-scanning microscopy was performed using an Ultima imaging system (Prairie Technologies, Middleton, WI, USA), a Ti:sapphire Chameleon Ultra femtosecond-pulsed laser (Coherent, Santa Clara, CA, USA) and $\times 60$ (0.9 NA) water-immersion IR objectives (Olympus, Center Valley, PA, USA). Calcium (Ca^{2+}) transients in presynaptic terminals were recorded using GCaMP6 expressed in the CA3 hippocampal neurons.

To express GCaMP6, mice were anesthetized using isoflurane (2% for induction and 1.5% for maintenance) in 100% oxygen, and their heads were restrained on a stereotaxic apparatus. An approximately 1-cm midline incision was made centered about 0.25 cm behind bregma. Viruses were injected into three locations within the CA3 region, in one or both hemispheres. The stereotaxic coordinates for the three injections were as follows, in relation to the bregma: (1) -1.5 mm anteroposterior, 1.8 mm lateral, and 1.7 mm deep; (2) 2.2 mm anteroposterior, 2.3 mm lateral and 1.8 mm deep; (3) 2.5 mm anteroposterior, 2.8 mm lateral and 2.2 mm deep. Craniotomy holes were drilled at these locations, and 200 nl of AAVs was slowly (20 nl min^{-1}) injected via a 33G cannula. After each injection, the cannula was left in place for 2–3 min before being retracted. Following injections, the skin was sutured, and the mice were allowed to recover before returning to the holding cages. Imaging experiments were performed 4–7 weeks after AAV injections. During each experiment, care was taken to limit the differences in post-injection durations to a maximum of 2–3 days across experimental groups to avoid substantial differences in the levels of AAV expression.

To visualize GCaMP6 or mitoGCaMP6, we used brain slices prepared from AAV-injected mice. Schaffer collaterals were stimulated via field stimulation using bipolar stimulating electrodes, as in STP experiments. In addition to D-AP5 and picrotoxin, the AMPA receptor antagonist NBQX ($3 \mu\text{M}$) was added to the bath ACSF to prevent excitation of postsynaptic neurons. GCaMP6 was visualized at 940 nm, and mCherry was visualized at 1040 nm by two Ti:Si lasers. Presynaptic boutons were identified in a $34 \mu\text{m} \times 34 \mu\text{m}$ region of interest by activity-dependent increase in GCaMP6 fluorescence during time-series scans. Line-scans through identified boutons were then used for experiments. Boutons from 4 to 8 regions of interests in the stratum radiatum of the CA1 area were imaged for each mouse. In some experiments, we used whole-cell recordings from CA3 neurons and filled the cells with Alexa Fluor 594 ($30 \mu\text{M}$) and Fluo 5 F ($300 \mu\text{M}$) at 820 nm to visualize presynaptic Ca^{2+} . Axons emanating from the cell bodies were identified based on their morphology and lack of spines. Presynaptic terminals were identified as boutons in secondary and

tertiary axonal branches. Those axons could not be tracked beyond 200 μm from the CA3 cell bodies due to the limitation of the approach. APs were evoked by holding the cells at -70 mV (current clamp mode) and injecting depolarizing current (3.5–4.0 nA, 500 μs). We recorded Ca^{2+} transients in line-scan mode from 3 to 7 boutons per cell. For GCaMP6 or mitoGCaMP6 experiments, the baseline fluorescence (F_0) was used to calculate the change in signal ($\Delta F/F_0$). For Fluo 5F experiments, fluorescence changes ($\Delta G/R$) were quantified as an increase in Fluo 5F fluorescence (ΔG) normalized to the respective Alexa 594 fluorescence (R). Imaging experiments were done without blinding.

Two-photon glutamate uncaging

For two-photon glutamate uncaging (TGU), MNI glutamate (2.5 mM) was added to the recording ACSF. The timing and intensity of glutamate uncaging were controlled by TriggerSync (Prairie Technologies). In typical experiments, 0.2-ms pulses from a second Ti:sapphire Chameleon Ultra laser (720 nm) were delivered to the vicinity of a targeted dendritic spine, and TGU-evoked EPSCs (uEPSCs) were recorded. The duration and intensity of illumination of the uncaging laser were then adjusted to induce responses that mimicked spontaneous miniature EPSCs, which were recorded in CA1 neurons and averaged 10–15 pA. After the uncaging parameters (i.e., site, laser duration and laser intensity) were adjusted for a single spine, the parameters remained constant for the STP experiments on the particular spine. An 80-Hz train of 100 TGU pulses was delivered to a single dendritic spine to measure TGU-induced STP.

Electron microscopy

Mice were anesthetized with ethyl carbamate (1.5 g kg^{-1} , 25% solution, intraperitoneal) and perfused transcardially with phosphate-buffered saline for 1–2 min and then a fixative (2.5% glutaraldehyde and 2% paraformaldehyde in 0.2 M sodium cacodylate). Brains were isolated, stored at 4 °C overnight in the same fixative and sagittal sections (100- μm -thick) were prepared on a vibratome (Leica Biosystems, Buffalo Grove, IL, USA). Smaller regions ($\sim 500 \mu\text{m} \times 500 \mu\text{m}$) containing the stratum radiatum of the CA1 hippocampal region were processed for three-dimensional (3D) scanning electron microscopy. The samples were stained with a modified heavy-metal-staining method, processed through a graded series of alcohol and propylene oxide, and then embedded in Epon hard resin.³² Sections (0.5- μm -thick) were cut to determine the correct area and then coated with iridium in a Denton Desk II sputter coater (Denton Vacuum, Moorestown, NJ, USA). The 3D EM images were collected on a Helios Nanolab 660 Dualbeam system (FEI, Hillsboro, OR, USA). From the 3D stacks of electron micrographs ($10 \times 10 \times 10 \text{ nm}$ voxel size, 250–260 sections of 10-nm thickness and approximately $30 \times 20 \mu\text{m}$ area), synapses were identified based on the presence of postsynaptic densities and presynaptic vesicles. The mitochondria in presynaptic terminals were identified and counted manually.

For transmission electron microscopy, 100- μm -thick vibratome sections containing the CA1 stratum radiatum region were prepared as described above and fixed in 2.5% glutaraldehyde and 2% paraformaldehyde in 0.1 M sodium cacodylate buffer (pH 7.4). Sections were post fixed in 2% osmium tetroxide in 0.1 M sodium cacodylate buffer with 0.3% potassium ferrocyanide for 1.5 h. After rinsing in the same buffer, the sections were dehydrated through a series of graded ethanol and propylene oxide solutions, infiltrated and embedded in epoxy resin, and polymerized at 70 °C overnight. Thin sections (0.5 μm) were stained with toluidine blue for examination by light microscopy. Ultrathin sections (80 nm) were cut and imaged using a Tecnai F 20 FEG Electron Microscope (FEI) with a XR41 Camera (Advanced Microscopy Techniques, Woburn, MA, USA).

Mitochondrial DNA quantification

RNA was isolated from the hippocampus of 4-month-old mice by using the mirVana RNA isolation kit (Ambion, Life Technologies, Foster City, CA, USA). The SuperScript III reverse transcriptase kit (Invitrogen, Life Technologies) was used to synthesize cDNA from the following primers were used in the qPCR experiments: COI (5'-GCCCCAGATATAGCATTCCC-3' and 5'-GTTTCATCTGTTCTGCTCC-3'); ND2 (5'-CCCATTCCACTTCTGATTACC-3' and 5'-ATGATAGTAGAGTTGAGTAGCG-3'); 18 S (5'-TAGAGGGACAAGTGG CGTTC-3' and 5'-CGCTGAGCCAGTCAGTGT-3'). The ratio of mitochondrial (COI and ND2) transcripts to the nuclear 18S transcript was used to quantify relative mitochondrial DNA.

Mitochondrial respiration

Mice were decapitated, and their brains were dissected immediately in cold (4 °C) dissecting ACSF. Hippocampi were removed and washed in a mitochondrial isolation buffer containing 250 mM sucrose, 1 mg ml⁻¹ bovine serum albumin, 5 mM EDTA and 10 mM Tris-HCl at pH 7.4. A crude mitochondrial fraction was then isolated by differential centrifugation. Briefly, the hippocampal tissue was finely minced on a pre-chilled glass dish, washed several times, resuspended in 1 ml mitochondrial isolation buffer and homogenized in a 2-ml Dounce homogenizer (glass/glass, 5–7 runs in an ice bath). The homogenized tissue was centrifuged at 700 g for 5 min; the supernatant was then transferred to a new 1.5-ml tube and centrifuged at 7000 g for 10 min. The resulting pellet was washed in 1 ml mitochondrial isolation buffer and resuspended in 30 µl mitochondrial isolation buffer. The protein concentration in the pellet was typically 25–35 mg protein ml⁻¹. The mitochondrial integrity was tested by measuring the glutamate/malate-dependent respiratory control ratio (i.e., State III/State IV of respiration). The resulting mitochondrial samples were used immediately to measure respiration (mitochondrial oxygen consumption) and Ca²⁺-retention capacity.

Mitochondrial oxygen consumption was measured using a Clark-type electrode (Hansatech Instruments, Norfolk, UK) in a thermostatically controlled chamber equipped with a magnetic stirring device and a gas-tight stopper fitted with a narrow port for additions via a Hamilton microsyringe. Isolated mitochondria were placed in the respiration chamber at 37 °C in 0.4 ml respiration buffer (250 mM sucrose, 1 g l⁻¹ bovine serum albumin, 10 mM KH₂PO₄, 2.7 mM KCl, 3 mM MgCl₂, 40 mM HEPES, 0.5 mM EGTA, pH 7.1) to yield a final concentration of 0.5 mg ml⁻¹. State III respiration was stimulated by the addition of 2 mM ADP. Respiratory control ratios were obtained by dividing the rate of oxygen consumption in the presence of ADP (state III) by that in the absence of ADP (state IV). The measurement protocol involved sequential addition (with 5-min intervals) of 5 mM glutamate, 2.5 mM malate (activating the CII–CIII–CIV span), 1 µM rotenone, 10 mM succinate (activating the CII–CIII–CIV span), 1 µM antimycin A, 10 mM ascorbate, 0.4 mM TMPD (activating the CIV span) and 5 mM KCN. The rates of oxygen consumption were calculated online, as first derivatives of the dioxygen-content changes by manufacturer-provided software.

Quantitative real-time PCR

The cDNA was generated from 1 µg hippocampal RNA by using Super Script III (Life Technologies, Waltham, MA, USA). Primers for qPCR were as follows:

Hira: TCCGCCATCCATCAATTC and CTATCCTTACCAGCCTAG,
Cldn5: CGCAGACGACTTGGAAAGG and GCCAGCACAGATTCATACAC,
Mrpl40: CTGGTAGTAGAGATAGGTGGTG and GAGGAGCTGAACTTGAATCTG,
Ufd11: TCAAGCATGTATTCATCTGC and TTTATTTACAGTGACTCAGAAGG,
2510002D24Rik: GTGTTCCAGGTCAAGTAA and AGAAGGACAAGTGATAAGC,
Cdc45l: GATTTCCGAAGGAGTCTACG and TACTGGACGTGGTCAACACTGA.
Co1: GCCCCAGATATAGCATTCCC and GTTCATCCTGTTCCTGTCTCC,
Nd2: CCCATTCACCTTCTGATTACC and ATGATAGTAGAGTTGAGTAGCG,
18s: TAGAGGGACAAGTGCGGCTTC and CGCTGAGCCAGCTAGTGT.

We performed qPCR using SYBR green in an Applied Biosystems 7900HT Fast Real-time PCR system (Thermo Fisher Scientific, Waltham, MA, USA) and the standard protocol. A serial dilution of cDNA was used to generate a standard curve for each primer set, and this curve was used to calculate gene concentrations for each sample. All samples were run in triplicate.

Mouse behavior

Mature animals (16–20 weeks) were used for all behavior experiments.

Morris water maze. One hour prior to testing, animals were brought into the testing room and allowed to habituate. Testing was performed during the animal's inactive phase under dim-light conditions. Mice were allowed to navigate in the maze, and swim patterns were recorded with a video camera tracking system (HVS Image, Buckingham, UK) mounted above the pool. Animals learned to find a hidden, clear platform by using the standard spatial version of the Morris water maze task for four successive days. Each day, animals were given four 1-min trials from each starting position with an intertrial latency of 60 s. The order of the starting locations was counterbalanced each day by using a Latin-square design. A spatial learning (probe) trial was administered 1 h after the completion of spatial training. A spatial memory (probe) trial was administered 48 h after completion of the spatial learning. During both probe trials, the platform

was removed, and the mice received a single 1-min trial in which the animals tried to find the escape platform. These trials originated from the starting location that was the farthest from the platform's location throughout training. Mice also completed a nonspatial learning task at least 7 days after completion of the spatial protocol. In that task, mice were trained to find a black visible platform for two successive days. During day 1, the escape platform was located in the same position used during spatial training. The next day, the escape platform was moved to a new quadrant. Each day, the mouse was given four 1-min trials in the same manner that occurred during spatial training. To avoid hypothermia, immediately after each round of training and testing trials, animals were dried with paper towels and placed in warmed holding cages.

Delayed non-matched-to-position task. To motivate mice to complete the delayed non-matched-to-position task, they were subjected to water restriction for 2 days prior to testing. Specifically, mice were allowed 2 h of free access to water per day. Mice were weighed daily to ensure that weight decrease during deprivation did not surpass the recommended 20% loss. One hour prior to testing, animals were brought into the testing room and allowed to habituate. Testing was performed during the animal's inactive phase under well-lit lighting conditions. The testing apparatus consisted of a Y-maze (Clever Sys, Reston, VA, USA) with a start arm (20 cm × 16 cm × 7 cm; l × w × h) leading to two goal arms (20 cm × 16 cm × 7 cm). Mice were allowed to habituate to the maze and were given a positive reinforcer (i.e., Chocolate Yoohoo) before behavioral testing. To achieve this, mice were allowed to investigate the Y-maze baited with Yoohoo for 15 min. Maze habituation was performed for two consecutive days.

After maze habituation was complete and the animal had consumed the food rewards, we conducted a test of spatial working memory. First, the mouse was constrained in the start arm with a guillotine door. Next, a sample arm was determined at random and the choice arm was closed off with a guillotine door. There was a limit of two consecutive same-side sample arms in a 10-trial test. Both arms were then baited with 20 µl Yoohoo. The mouse was released from the start chamber and allowed to run to the sample arm and consume the reward. The mouse was then returned to the start arm and the guillotine door to the nonsample arm was removed. All efforts were made to keep the intratrial interval at 5 s. The mouse was again released from the start chamber and allowed to run to either the previously entered sample arm or new choice arm to consume the reward. A return to the sample arm was counted as an incorrect response. Incorrect responses resulted in no reward and return to the start arm. A total of 10 trials were given.

The Y-maze spatial recognition. The maze was shaped like a 'Y', with three equally spaced arms (20 cm × 7 cm × 16 cm) radiating from a triangular center section. The Y-maze was constructed from blue opaque plastic to aid in video detection. The maze was located in a lit room with abundant extra-maze cues. The procedure consisted of an acquisition and a recognition session. During the acquisition session, the mouse was placed facing the distal end of an arm (start arm; determined semirandomly) and allowed to freely explore the maze for 15 min. During acquisition, the mouse was allowed to freely explore two of the three arms (determined semirandomly). After completing the acquisition session, the mouse was returned to its home cage for 1 h. Next, the mouse was given a 2-min recognition session, where all three arms were available for the mouse to freely explore. Time spent in each arm and the triangular center section and the total distance traveled during each trial were automatically recorded using TopScan software (Clever Sys). Mice prefer novelty; therefore, if a mouse recognized and remembered which arms were familiar during the recognition session, the mouse would spend more time in the novel arm (expressed as a percent of total arm time) than would be expected by chance.

Acoustic startle and prepulse inhibition. Each day before testing, the mice were allowed a 1-h habituation in the testing room after being transported from the animal housing room. Before experiments were initiated, the mice were allowed to acclimate to the Plexiglas restraint chamber (6 cm × 6 cm × 4.8 cm) for 20 min. Acoustic startle and prepulse inhibition (PPI) tests were performed in ventilated, sound-attenuated chambers (Med Associates, St. Albans City, VT, USA). For acoustic-startle experiments, the mice had a 5-min acclimation period to a 65-dB background white noise, which played throughout the session. Three startle pulses (8 kHz, 120 dB, 40 ms) were then delivered at 15-s intertrial intervals.

For PPI experiments (conducted on different days than acoustic-startle experiments), mice had a 5-min acclimation period to a 65-dB background

white noise, which played throughout the session. Three acoustic startles (broadband white noise click, 120 dB, 40 ms) were then delivered separated by a 15-s intertrial interval. The testing session consisted of 39 trials of 5 trial types: pulse alone, in which the startle pulse was presented; the combination of a 40-ms prepulse of 74, 82 or 90 dB preceding the startle pulse by 100 ms; and no stimuli. Trials were separated by 15 s and presented in a pseudo-random order. PPI was calculated as follows: $100 \times (\text{pulse-alone response} - \text{prepulse} + \text{pulse response}) / \text{pulse-alone response}$. All mouse behavior experiments were performed in a blind manner in respect to mouse genotypes.

Western blotting

AAV5-*hSyn-mCherry-2A-mitoGCaMP6f* or AAV5-*hSyn-mCherry-2A-GCaMP6f* viruses were injected *in vivo* into the mouse hippocampus as described above. Four weeks after injections, mice were killed and dorsal hippocampi were isolated at 4 °C for fractionation into nuclear/cell debris, cytoplasm and crude mitochondrial fractions. Freshly extracted hippocampi from each mouse were homogenized in isolation buffer (250 mM sucrose, 75 mM mannitol, 1 mM EGTA and 5 mM HEPES, at pH 7.4) by using a glass-teflon tissue homogenizer on ice. Homogenized hippocampi were centrifuged twice at 1400 g for 3 min at 4 °C to separate nuclei and cell debris. The supernatant was then centrifuged at 17 200 g for 10 min at 4 °C to separate cytosol and crude mitochondria. Ice-cold RIPA buffer (Santa Cruz Biotechnology, Dallas TX, USA) with protease inhibitors (Roche, Basel, Switzerland) was added to the mitochondria but not the cytoplasmic fraction, and both were briefly sonicated. Samples were centrifuged at 17 200 g for 20 min at 4 °C, and the pellet was kept at -80 °C for protein quantification. Protein quantification was performed using a Pierce BCA Protein Assay Kit (Thermo Scientific, Waltham, MA, USA). For loading-sample preparation, we used NuPAGE LDS sample buffer (Life Technologies, Thermo Fisher Scientific).

The western blot experiments were performed similar to a previously described method.¹² Briefly, NuPAGE 10% Bis-Tris gels and MES-SDS running buffer (Life Technologies) were used to load mitochondria and cytoplasmic fractions (10 µg total protein/well) and run the gels. The primary antibody used to detect GCaMP6 was rabbit-anti-GFP (1:1000; Abcam, 6556, Cambridge, MA, USA). We also used rabbit-anti-Prohibitin 1 (1:1000; Thermo Scientific, PA5-12274) and mouse-anti-β-actin (1:10 000; Sigma-Aldrich, 5316, St. Louis, MO, USA) primary antibodies. Secondary antibodies were Odyssey goat-anti-rabbit IRDye-680LT (1:40 000; LI-COR Biosciences, Lincoln, NE, USA, 926-68021) or Odyssey donkey-anti-mouse IRDye-800CW (1:15 000, LI-COR Biosciences, 926-32212). Membranes were imaged using an Odyssey Infrared Imager (LI-COR Biosciences). Images were analyzed using Odyssey V3.0 software (LI-COR Biosciences).

Subcellular localization of mitoGCaMP6 and GCaMP6

Neuro-2a (N2a) mouse neuroblastoma cells (ATCC, CCL-131, Manassas, VA, USA) were plated in four-well chamber slides (Lab-Tek 177399, Thermo-Fisher Scientific) at 1.25×10^5 cells/well and maintained in culture using Eagle's medium essential media (ATCC) plus 10% fetal bovine serum (heat inactivated; Life Technologies) and $1 \times$ PenStrep (Life Technologies) in an incubator at 37 °C and 95% O₂/5% CO₂. Following a 24-h incubation, cells were transfected with *hSyn-mCherry-2A-mitoGCaMP6f* or *hSyn-mCherry-2A-GCaMP6f* plasmids (0.5 µg DNA/well) using Fugene HD transfection reagent (Promega, Madison, WI, USA) (Ration Fugene HD/DNA 1:4) in serum-free Eagle's medium essential media. Twenty-four hours later, cells were supplemented with additional fresh complete media, and 48 h later, they were incubated in complete media with Mitotracker DeepRed (1:2000, Life Technologies) for 15 min at 37 °C. Next, Mitotracker was washed out and replaced with fresh complete media, and cells were placed back to the incubator for 15–20 min. Cells were then washed with sterile phosphate-buffered saline and fixed in 4% paraformaldehyde for 15 min at room temperature. Following fixation, cells were washed three times for 5 min with phosphate-buffered saline and blocked with 10% normal goat serum and 0.1% TritonX-100 in phosphate-buffered saline for 1 h at room temperature. We used the following antibodies: chicken-anti-GFP to detect GCaMP6 or mitoGCaMP6 (1:1000; Abcam, 13970) and goat-anti-chicken-Alexa-488 (1:1000; Life Technologies, A11039). Cell imaging was performed using an LSM-780 confocal microscope (Zeiss, Oberkochen, Germany).

Other drugs and chemicals

Bongkrekic acid (BKA) solution was purchased from Sigma-Aldrich. D-AP5, picrotoxin, tetrodotoxin, NBQX, CGP 37157, MNI glutamate were from Tocris (Minneapolis, MN, USA). Stock solutions of these drugs were prepared in manufacturer-recommended solvents and stored at -20 °C. Ru360 was from Calbiochem (San Diego, CA, USA).

Statistical analyses

Data are presented as the mean ± s.e.m. Statistical analyses were performed using SigmaPlot software (Systat Software, San Jose, CA, USA). Parametric or nonparametric tests were chosen based on the normality and variance of data distribution. Independent or paired two-tailed *t*-tests (*t*-value), Mann-Whitney rank-sum test (*U* value), one-way analysis of variance (ANOVA)/Kruskal-Wallis one-way analysis of variance on ranks followed by a multiple comparison procedure (Dunn's method), two-way ANOVA/two-way repeated measures ANOVA with one factor repetition followed by Holm-Sidak multiple comparison procedure were the statistical tests used. *F*-values were reported for ANOVA and *Q*-values from multiple comparison procedure were reported for ANOVA on ranks. Differences with *P* < 0.05 were considered significant.

RESULTS

Abnormal presynaptic augmentation underlies aberrant STP in *Df(16)5^{+/-}* mice

To determine whether haploinsufficiency of distal genes in the 22q11DS region contributes to hippocampal pathophysiology, we used *Df(16)5^{+/-}* mice³³ carrying a hemizygous deletion of six genes: *Cldn5*, *Cdc45l*, *Ufd1l*, *2510002D24Rik*, *Mrpl40* and *Hira* (Figure 1a). Similar to the late onset of SCZ symptoms, synaptic plasticity abnormalities in mouse models of 22q11DS do not appear until later in life;²³ thus, we used 4- to 5-month-old mice for these experiments. *Df(16)5^{+/-}* mice developed normally and had no visible gross morphologic abnormalities (data not shown).

Using the whole-cell voltage-clamp technique, we recorded excitatory postsynaptic currents (EPSCs) at glutamatergic synapses between CA3 and CA1 pyramidal neurons in the hippocampus (CA3–CA1 synapses) by electrically stimulating Schaffer collaterals. Basal synaptic transmission measured as the input–output relation between stimulation intensity and EPSCs in *Df(16)5^{+/-}* mice was comparable to that of WT littermates ($F_{(1,12)} = 1.435$, $P = 0.231$) (Figure 1b). EPSC kinetics, such as rise time ($t_{(19)} = 0.442$, $P = 0.663$), half-width ($U = 51$, $P = 0.805$) and decay time ($t_{(19)} = 0.0377$, $P = 0.970$) were also normal between mutants and controls (Supplementary Figure S1). However, an 80-Hz train (100 stimuli) applied to Schaffer collaterals evoked a substantially larger STP ($t_{(16)} = 2.196$; $P = 0.010$) in *Df(16)5^{+/-}* mutants than in WT mice (Figure 1c). Because STP is not a unitary process but rather consists of several temporally and mechanistically distinct components (e.g., facilitation, augmentation and depression of presynaptic transmission²⁰), we measured STP components individually.

The STP increase in *Df(16)5^{+/-}* mutants could arise from the increased facilitation/augmentation, decreased short-term depression or a combination thereof.²¹ To differentiate among these possibilities, we used an established protocol to separate STP components²⁹ and assess their individual contributions to the STP increase in *Df(16)5^{+/-}* mice. First, using the paired-pulse ratios of two consecutive EPSCs, we found no significant difference ($F_{(1,5)} = 2.142$, $P = 0.146$) in facilitation between *Df(16)5^{+/-}* and WT mice (Figure 1d). We then examined whether the increased STP in *Df(16)5^{+/-}* mice resulted from reduced short-term depression. We examined the recovery from depression by using a 5-Hz stimulus train applied during the first 5 s after the 80-Hz train of Schaffer collateral stimuli. Because recovery from depression overlaps with the decay of augmentation during those 5 s, the actual EPSC peak amplitude reflects the net effect of the two processes.²¹ To isolate the depression component, we corrected the synaptic responses for contribution from augmentation^{21,29}

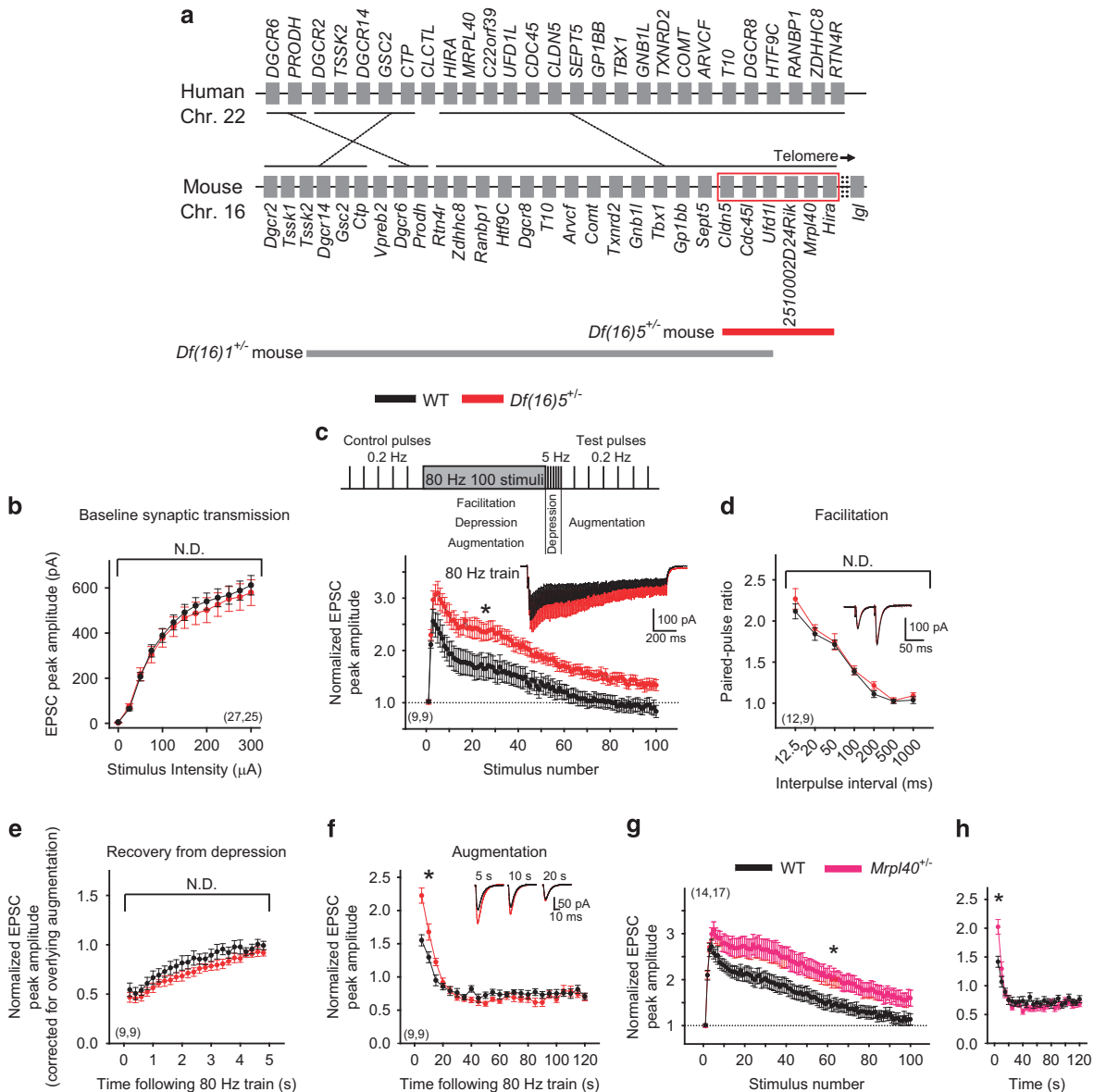


Figure 1. Abnormal short-term synaptic plasticity in $Df(16)5^{+/-}$ mice is caused by $Mrpl40$ haploinsufficiency. **(a)** Diagram depicting genes in the 22.q11.2 genomic region of the human chromosome 22 and the syntenic region of mouse chromosome 16. Red horizontal bar represents genomic regions hemizygotously deleted in $Df(16)5^{+/-}$ mice, and gray horizontal bar represents genomic regions hemizygotously deleted in $Df(16)1^{+/-}$ mice. Note that *2510002D24Rik*, *Mrpl40* and *Hira* genes are mapped outside the *Df(16)1* microdeletion. **(b)** Input-output relations in $Df(16)5^{+/-}$ and wild-type (WT) littermates. **(c)** Short-term potentiation (STP, comprising facilitation, depression and augmentation) induced by the high-frequency (80 Hz) train. The first time point represents an average of five baseline excitatory postsynaptic currents (EPSCs) delivered at low frequency. The top inset shows the protocol for measuring STP, recovery from depression and augmentation in the same experiment. **(d-f)** Average facilitation tested by paired-pulse ratio in separate experiments **(d)**, recovery from depression tested 5 s after the 80-Hz train **(e)** and augmentation tested 5–120 s after the 80-Hz train in $Df(16)5^{+/-}$ and WT mice **(f)**. Insets show representative EPSC traces. **(g, h)** Mean STP of EPSCs induced by the 80-Hz train of synaptic stimulation of Schaffer collaterals **(g)** and augmentation **(h)** in $Mrpl40^{+/-}$ mice and their WT littermates. Numbers of neurons are shown in parentheses. N.D., not significantly different. Data are represented as mean \pm s.e.m. * $P < 0.05$.

(see Supplementary Methods). This analysis revealed no significant difference ($F_{(1,23)} = 1.947$; $P = 0.182$) in recovery from short-term depression between $Df(16)5^{+/-}$ and WT littermates (Figure 1e).

Next, we assessed the role of augmentation, which is the longest-lasting component of STP and operates on a time scale of tens of seconds.²⁹ Using a previously reported approach,²⁹ we isolated augmentation by applying a single stimulus to Schaffer collaterals every 5 s for 2 min, starting 5 s after the 80-Hz train (Figure 1f). Augmentation was significantly increased ($t_{(16)} = 4.758$, $P = 0.0002$) in $Df(16)5^{+/-}$ mice compared with WT controls

(Figure 1f). This increased augmentation in $Df(16)5^{+/-}$ mice was maximal at the onset and decayed to normal values after 20 s. Elevated augmentation in $Df(16)5^{+/-}$ mutants was not sensitive to the Serca inhibitor thapsigargin (4 μ M) (without thapsigargin: $t_{(16)} = 4.404$, $P < 0.001$; with thapsigargin: $t_{(10)} = 1.954$, $P = 0.0396$) (Supplementary Figure S2a). Further, Serca2 protein levels were normal ($U = 107$, $P = 0.836$) in $Df(16)5^{+/-}$ mice (Supplementary Figure S2b), suggesting that haploinsufficiency of genes within the *Df(16)5* genomic region resulted in abnormal STP through Serca2-independent mechanisms. To ensure that the STP increase in $Df(16)5^{+/-}$ mice originated from the presynaptic CA3 neurons, we

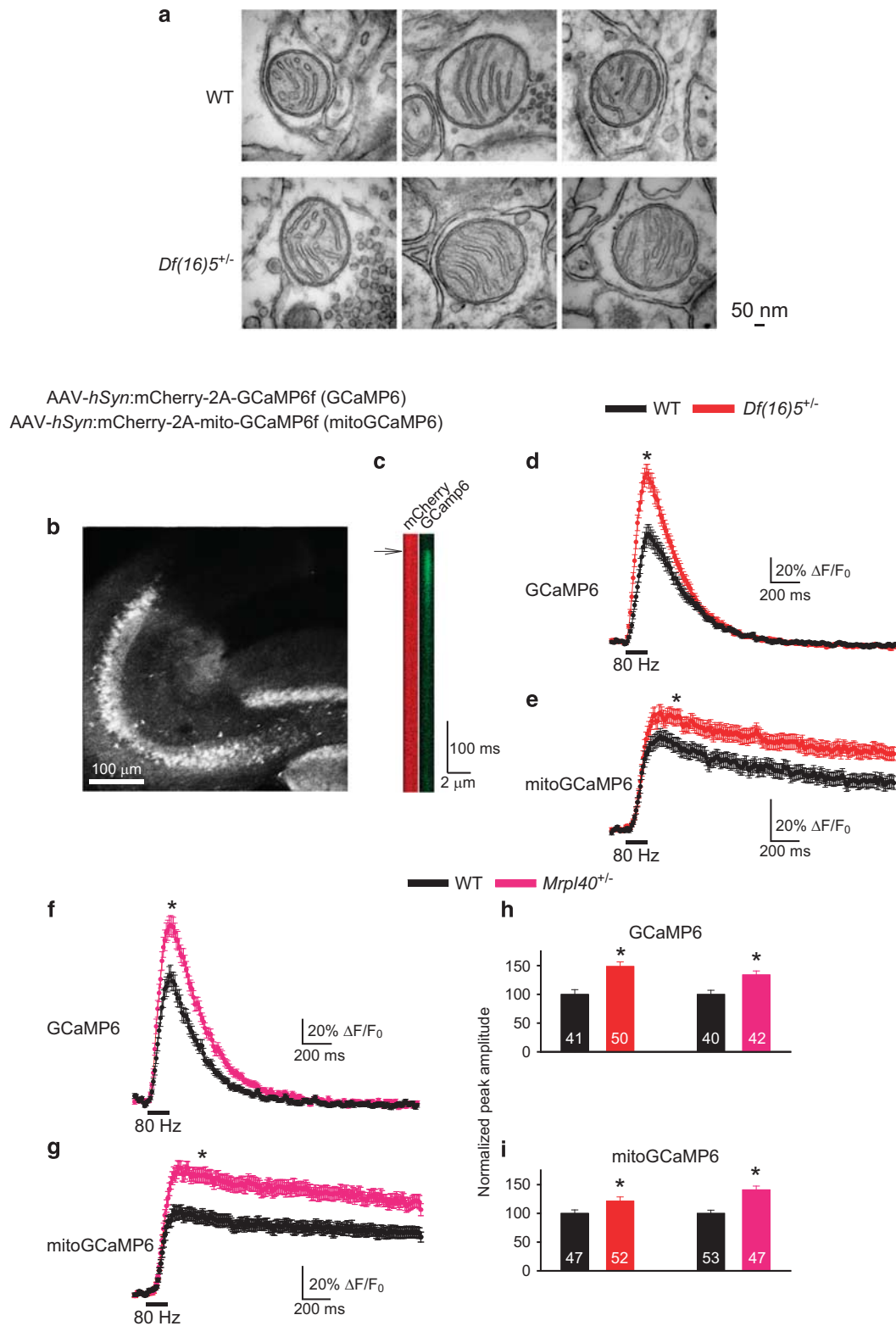


Figure 2. Normal mitochondrial structure but abnormal presynaptic cytosolic and mitochondrial calcium regulation in *Df(16)5^{+/-}* and *Mrpl40^{+/-}* mice. **(a)** Three representative transmission electron microscopy images of mitochondrial ultrastructure in the CA1 area of the hippocampus of wild-type (WT) and *Df(16)5^{+/-}* mice. **(b)** The representative fluorescent image of mCherry after infection of the CA3 area with adeno-associated viruses (AAVs) encoding either GCaMP6 or mitoGCaMP6. **(c)** Line scan of mCherry and GCaMP6 fluorescence in a CA3 presynaptic terminal before and after the 80-Hz stimulation of Schaffer collaterals (arrow). **(d–g)** Mean normalized cytosolic GCaMP6 **(d, f)** and mitoGCaMP6 **(e, g)** fluorescence in CA3 presynaptic terminals imaged in the CA1 area of the hippocampus, before and after 80-Hz stimulation in *Df(16)5^{+/-}* and WT littermates **(d, e)** and *Mrpl40^{+/-}* and WT littermates **(f, g)**. **(h, i)** Normalized mean peak amplitudes of GCaMP6 **(h)** or mitoGCaMP6 **(i)** in *Df(16)5^{+/-}* and WT littermates and *Mrpl40^{+/-}* and WT littermates. Numbers of fluorescent puncta are shown inside columns. **P* < 0.05.

examined the role of the postsynaptic component by performing TGU (100 TGU pulses, 80 Hz) to activate individual dendritic spines on CA1 neurons, the postsynaptic sites of CA3 inputs. Because TGU focally releases exogenous glutamate from inactive (caged) glutamate (MNI glutamate), thereby bypassing the release of endogenous neurotransmitter from CA3 terminals, this method tests only postsynaptic mechanisms of synaptic transmission and plasticity. TGU-induced STP did not differ ($t_{(25)} = -0.405$, $P = 0.689$) between *Df(16)5^{+/-}* and WT littermates (Supplementary Figure S3a), suggesting that the causative locus of the abnormal STP increase in *Df(16)5* mutants resides in the presynaptic CA3 neurons. CA3 pyramidal neuron recordings revealed that presynaptic neurons had normal resting membrane potential ($t_{(18)} = -1.621$, $P = 0.122$), input resistance ($t_{(18)} = 0.978$, $P = 0.341$) and depolarization-induced APs (rheobase: $t_{(18)} = 0.451$, $P = 0.658$; AP width: $t_{(18)} = 0.384$, $P = 0.706$) (Supplementary Figure S3b). An 80-Hz train of depolarization pulses delivered to the CA3 soma progressively increased the AP width, but to the same extent (100th AP width: $t_{(12)} = 0.845$, $P = 0.414$) in both *Df(16)5^{+/-}* and WT littermates (Supplementary Figures 3c and d), thereby ruling out CA3 excitability as the culprit mechanism and implicating abnormal presynaptic glutamate release as a possible underlying mechanism of elevated STP in *Df(16)5^{+/-}* mice.

Mrpl40 haploinsufficiency causes abnormal STP in *Df(16)5^{+/-}* mice
To identify the culprit gene(s) whose haploinsufficiency causes abnormal augmentation and STP in *Df(16)5^{+/-}* mice, we tested STP parameters in *Cldn5^{+/-}* and *Hira^{+/-}* mice^{27,28} and the following new mutants that we generated: *Cdc45^{+/-}*, *Ufd1^{+/-}*, *2510002D24Rik^{+/-}* and *Mrpl40^{+/-}* mice (Supplementary Figure S4). All transcripts were reduced by approximately 50% in the *Df(16)5^{+/-}* mice (*Cldn5^{+/-}*: $P < 0.001$; *Cdc45^{+/-}*: $P = 0.03$; *Ufd1^{+/-}*: $P = 0.004$; *2510002D24Rik^{+/-}*: $P = 0.005$; *Mrpl40^{+/-}*: $P = 0.010$; *Hira^{+/-}*: $P = 0.003$) and the respective individual mutants (*Cldn5^{+/-}*: $P < 0.001$; *Cdc45^{+/-}*: $P < 0.001$; *Ufd1^{+/-}*: $P < 0.001$; *2510002D24Rik^{+/-}*: $P = 0.004$; *Mrpl40^{+/-}*: $P < 0.001$; *Hira^{+/-}*: $P = 0.03$) (Supplementary Figure S4).

Testing STP in all six mouse mutants revealed that *Mrpl40^{+/-}* mice had elevated STP and augmentation compared with their WT littermates (STP: $t_{(29)} = 2.368$, $P = 0.025$; augmentation: $t_{(29)} = 3.150$, $P = 0.0037$), whereas *Cldn5^{+/-}*, *Cdc45^{+/-}*, *Ufd1^{+/-}*, *2510002D24Rik^{+/-}* and *Hira^{+/-}* mutants had normal STP and augmentation (STP and augmentation, respectively: *Cldn5^{+/-}*: $t_{(12)} = 0.349$, $P = 0.733$ and $t_{(12)} = -1.205$, $P = 0.250$; *Cdc45^{+/-}*: $t_{(18)} = 0.566$, $P = 0.579$ and $t_{(18)} = -0.637$, $P = 0.532$; *Ufd1^{+/-}*: $U = 43$, $P = 0.903$ and $U = 35$, $P = 0.438$; *2510002D24Rik^{+/-}*: $t_{(35)} = 0.789$, $P = 0.436$ and $t_{(35)} = 1.773$, $P = 0.085$; *Hira^{+/-}*: $t_{(11)} = -0.644$, $P = 0.532$ and $t_{(11)} = -0.687$, $P = 0.507$) (Figures 1g and h and Supplementary Figure S5). *Mrpl40* haploinsufficiency did not affect mRNA expression of other genes in the *Df(16)5* microdeletion (*Gapdh*: $U = 28$, $P = 0.871$; *Mrpl40*: $t_{(14)} = 4.225$, $P < 0.001$; *Cldn5*: $t_{(14)} = -0.0174$, $P = 0.986$; *Ufd1*: $t_{(14)} = -0.368$, $P = 0.719$) (Supplementary Figure S6). The full complement of the *Mrpl40* gene appeared to be essential for prenatal development as its homozygous deletion was embryonically lethal. The enhanced STP and augmentation in *Mrpl40^{+/-}* mice were comparable to those in *Df(16)5^{+/-}* mice, suggesting that hemizygous deletion of *Mrpl40* underlies the abnormal synaptic plasticity in *Df(16)5^{+/-}* mice.

Df(16)5 deletion does not disrupt mitochondrial structure or oxidative phosphorylation

Because *Mrpl40* is thought to be one of the proteins of the mitoribosome complex,^{34,35} we investigated whether mitochondrial numbers, structure or function were affected in *Df(16)5^{+/-}* mice. We found no significant difference in mitochondrial ultrastructure imaged with transmission electron microscopy in the CA1 area of the hippocampus (Figure 2a), in total

mitochondrial DNA (*Co1*: $U = 89$, $P = 0.147$; *Nd2*: $U = 101$, $P = 0.318$) or in oxidative phosphorylation ($F_{(1,8)} = 0.108$, $P = 0.745$) in isolated mitochondria from the hippocampus between *Df(16)5^{+/-}* and WT littermates, suggesting normal energy production in mice with a *Df(16)5* hemizygous deletion (Supplementary Figure S7). Furthermore, 3D scanning electron microscopy imaging of the hippocampal CA1 area revealed a normal distribution of mitochondria in presynaptic terminals of *Df(16)5^{+/-}* mice compared with WT littermates ($U = 34.5$, $P = 0.093$) (Supplementary Figure S8), suggesting normal trafficking of mitochondria to presynaptic terminals in *Df(16)5^{+/-}* mice.

Dysregulation of activity-dependent presynaptic and mitochondrial Ca^{2+} in *Mrpl40^{+/-}* mice

Because mitochondria also regulate presynaptic Ca^{2+} levels, we measured activity-dependent Ca^{2+} changes in response to the 80-Hz stimulation of Schaffer collaterals in presynaptic CA3 terminals in the hippocampal stratum radiatum (CA1 area). To this end, we took advantage of the highly sensitive genetically encoded Ca^{2+} indicator GCaMP6f (GCaMP6).²⁵ After infecting the CA3 area of the hippocampus *in vivo* with recombinant AAVs encoding mCherry and GCaMP6, we observed high expression of fluorescent proteins in neuronal cell bodies in the CA3 area but not in the CA1 area (Figure 2b). In the stratum radiatum we observed fluorescent boutons, which responded to 80-Hz electrical stimulation (10 pulses) of Schaffer collaterals with GCaMP6 fluorescence transients with fast rise and decay (rise time_{20-80%}, 100.46 ± 4.03 ms; decay time (τ), 222.71 ± 9.40 ms) (Figure 2c). These activity-dependent kinetics of GCaMP6 fluorescence were similar to those observed in CA3 presynaptic terminals in which the inorganic Ca^{2+} indicator Fluo 5F was used (data not shown), suggesting that GCaMP6 reliably measures cytosolic Ca^{2+} in presynaptic terminals. The activity-dependent increase in GCaMP6 fluorescence during the 80-Hz train of stimulations was substantially higher ($U = 537$, $P < 0.001$) in *Df(16)5^{+/-}* mice than in their WT littermates (Figure 2d), which is consistent with the notion that higher presynaptic Ca^{2+} levels lead to elevated augmentation and STP.²⁰

To directly measure Ca^{2+} in the mitochondria of CA3 axons and terminals, we expressed GCaMP6 with a mitochondrial-localization signal (mitoGCaMP6) in the CA3 area using recombinant AAVs and imaged in the CA1 area (Figure 2b). We verified the specific localization of mitoGCaMP6 to mitochondria using subcellular fractionation followed by western blotting and co-immunolocalization with mitochondrial markers (Supplementary Figure S9). We also verified that the activity-dependent increase in mitoGCaMP6 fluorescence was sensitive to an inhibitor of the mitochondrial Ca^{2+} uniporter Ru360 (10 μ M) ($U = 15$, $P < 0.001$) (Supplementary Figure S10). An 80-Hz train (10 pulses) applied to the Schaffer collaterals induced an activity-dependent increase in mitoGCaMP6 but with substantially slower kinetics compared with cytosolic GCaMP6 (mitoGCaMP6: rise time_{20-80%}, 210.21 ± 27.03 ms, decay time > 1 s; GCaMP6: rise time_{20-80%}, 100.46 ± 4.03 ms; decay time (τ), 222.71 ± 9.40 ms; $U = 540$, $P < 0.001$) (Figure 2e). Similar to cytosolic Ca^{2+} , mitochondrial Ca^{2+} was elevated ($U = 889$, $P = 0.020$) in *Df(16)5^{+/-}* mice in response to the 80-Hz synaptic stimulation (Figure 2e). The increases in cytosolic and mitochondrial Ca^{2+} were also observed in *Mrpl40^{+/-}* mice to a similar degree as in *Df(16)5^{+/-}* mice (GCaMP6: $U = 482$, $P < 0.001$; mitoGCaMP6: $U = 618$, $P < 0.001$) (Figures 2f–i). These data suggest that *Mrpl40* is the gene in the *Df(16)5* genomic region that is responsible for the STP phenotype by deregulating activity-dependent mitochondrial and cytoplasmic presynaptic Ca^{2+} dynamics.

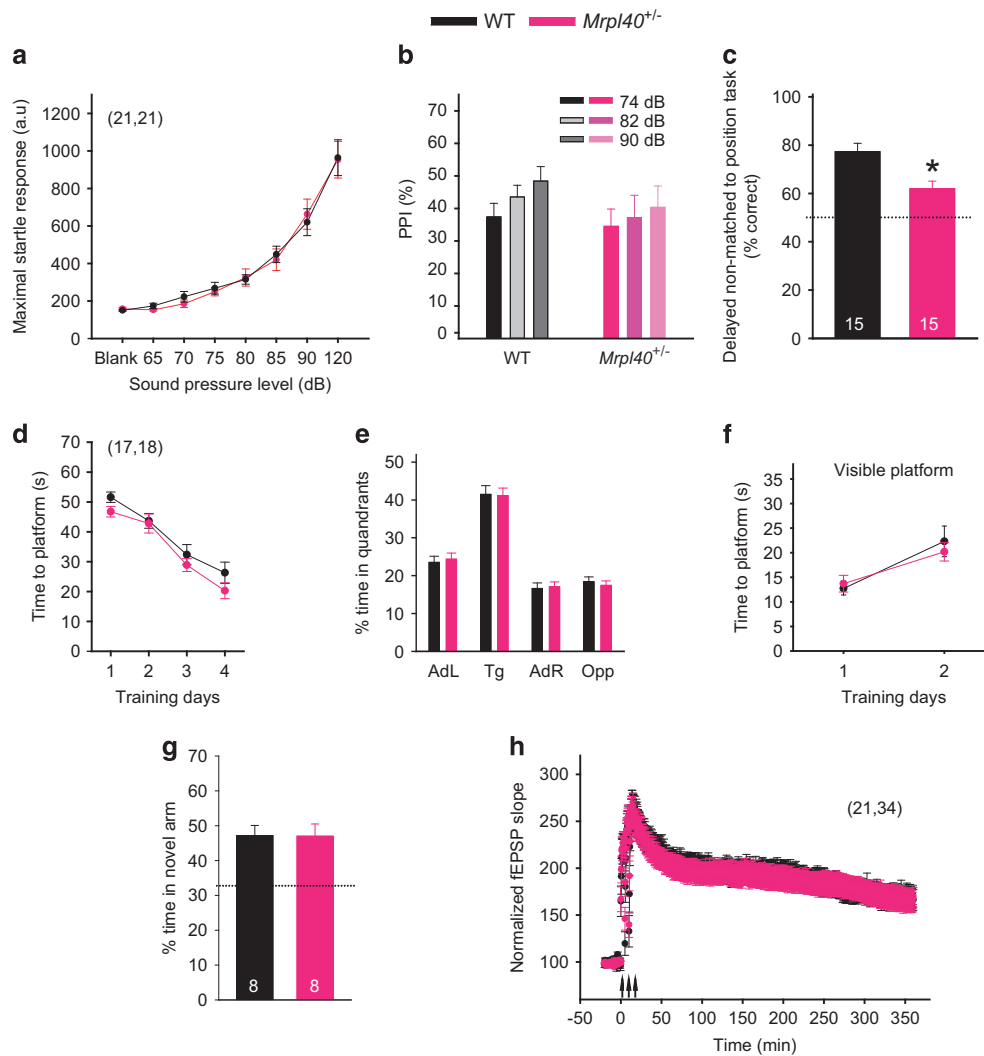


Figure 3. Deficient working memory and normal long-term spatial memory, long-term synaptic plasticity and acoustic startle in *Mrpl40*^{+/-} mice. **(a, b)** Mean maximal startle responses as a function of sound intensity **(a)** and prepulse inhibition (PPI) **(b)** in *Mrpl40*^{+/-} and wild-type (WT) littermates. **(c)** The mean numbers of correct choices made in the delayed non-matched-to-position task by *Mrpl40*^{+/-} and WT littermates. **(d–f)** Morris water maze tasks. Average time to find a submerged platform during the learning phase **(d)**, time spent in quadrants during the probe test performed 48 h after the last learning session **(e)** and time to travel to a visible platform **(f)** in *Mrpl40*^{+/-} and WT littermates. Abbreviations: AdL, adjacent left quadrant; AdR, adjacent right quadrant; Opp, opposite quadrant; Tg, target quadrant. **(g)** Average percentage of time spent in the novel arm in the novel-recognition version of the Y-maze task by *Mrpl40*^{+/-} and WT mice. **(h)** Long-term potentiation at CA3–CA1 synapses measured as mean field EPSP (fEPSP) as a function of time before and after tetanization of Schaffer collaterals with 200-Hz trains (arrows) in *Mrpl40*^{+/-} and WT mice. Dashed lines in **(c, g)** indicate the level of performance expected by chance. Numbers of mice or slices are shown in parentheses or inside columns. **P* < 0.05.

Mrpl40^{+/-} mice are deficient in short-term but not long-term spatial memory or long-term synaptic plasticity

To test if the hemizygous *Mrpl40* deletion affects cognitive function, we compared the performance of *Mrpl40*^{+/-} and WT mice in several behavioral tests. *Mrpl40*^{+/-} mice behaved normally in the acoustic startle ($F_{(1,7)}=0.0711$, $P=0.79$) and PPI ($F_{(1,2)}=1.314$, $P=0.274$) of acoustic-startle tests (Figures 3a and b), a measure of sensorimotor gating that is believed to be associated with positive symptoms of SCZ.³¹ To test spatial working memory, we used a delayed, non-matched-to-position task, in which timing between runs ranged from 0 to 5 s. In this test, *Mrpl40*^{+/-} mice performed significantly worse ($t_{(28)}=3.3$, $P=0.003$) than WT littermates (Figure 3c). However, *Mrpl40*^{+/-} mice performed normally in the tasks that assessed long-term memory (e.g., Morris water maze task). In this task, mutant mice

learned to find the invisible escape platform (Figure 3d) and retained this spatial memory for 48 h similar to WT controls ($F_{(1,3)}=0.0425$, $P=0.837$; Figure 3e). *Mrpl40*^{+/-} mice also performed comparably to WT controls (day 1: $t_{(33)}=-0.457$, $P=0.651$; day 2: $U=149.5$, $P=0.921$) when the escape platform was visible (Figure 3f). *Mrpl40*^{+/-} mutants also showed no memory deficits in the Y-maze ($t_{(14)}=0.160$, $P=0.873$), where we measured the amount of time a mouse spends in a novel arm 1 h after exploring the other two arms of the maze (Figure 3g).

These data suggest that *Mrpl40* haploinsufficiency affects short-term (working) memory but not long-term memory. Consistent with this notion, STP was abnormal in *Mrpl40*^{+/-} mice (Figures 1g and h), but long-term potentiation of excitatory synaptic transmission, a major form of long-term synaptic plasticity at CA3–CA1 synapses, did not differ ($t_{(53)}=0.161$, $P=0.873$) between *Mrpl40*^{+/-} mice and WT littermates (Figure 3h).

Mitochondrial Ca²⁺-extrusion deficit underlies STP and Ca²⁺ phenotypes in *Mrpl40*^{+/-} mice

The abnormally high increase in cytoplasmic Ca²⁺ induced by the 80-Hz synaptic stimulation in *Mrpl40*^{+/-} mice coincided with the enhanced mitochondrial Ca²⁺ increase. A role for slow mitochondrial Ca²⁺ extrusion in STP has been implicated in the crayfish neuromuscular junction³⁶ and led us to hypothesize that our results in the hippocampus could also be explained by impaired Ca²⁺ extrusion from mitochondria. Two major mechanisms extrude Ca²⁺ from the mitochondrial matrix to the cytoplasm: mitochondrial Ca²⁺ exchangers and the mPTP.^{37,38} The selective antagonist of the mitochondrial Na⁺-Ca²⁺ exchanger, CGP 37157 (5 μM), had no effect on STP or augmentation in WT mice (STP: $t_{(18)} = 0.999$, $P = 0.333$; augmentation: $t_{(18)} = 1.007$, $P = 0.330$), suggesting that this Ca²⁺ extrusion mechanism is not required for Ca²⁺ handling by mitochondria during 80-Hz-induced synaptic plasticity (Supplementary Figure S11). However, BKA (2 μM), a non-selective inhibitor of the adenine nucleotide (ADP/ATP) translocases (ANTs),³⁹ which are required for sensitivity of mPTP to calcium,⁴⁰ significantly increased STP and augmentation (STP: $U = 14$, $P = 0.005$; augmentation: $t_{(19)} = -3.169$, $P = 0.005$) in WT mice (Figure 4a and Supplementary Figures S12a and c). This increase mimicked the STP and augmentation enhancement in *Df(16)5*^{+/-} and *Mrpl40*^{+/-} mice. Interestingly, BKA did not increase STP or augmentation further (STP: $t_{(19)} = -0.107$, $P = 0.916$; augmentation: $t_{(19)} = -0.928$, $P = 0.365$) in *Df(16)5*^{+/-} mice

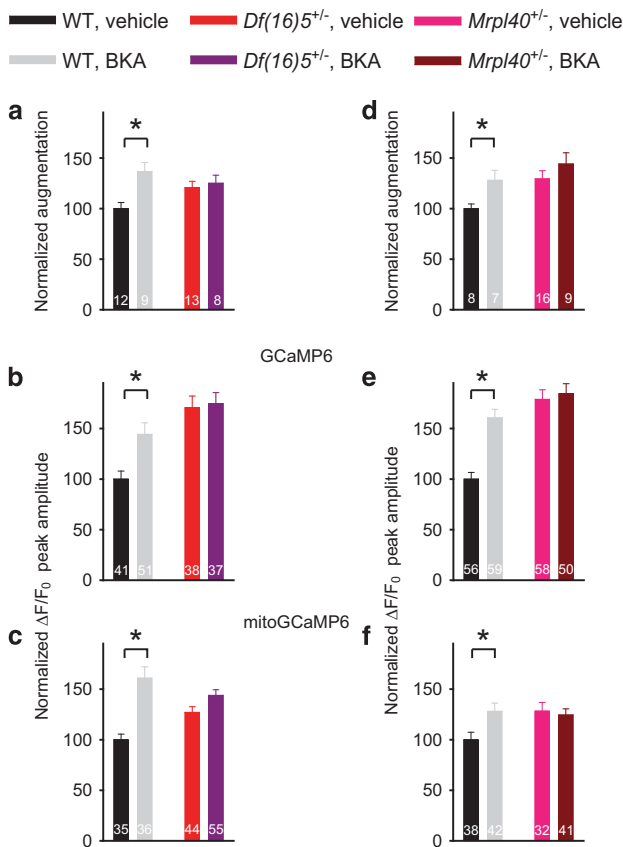


Figure 4. The mitochondrial permeability transition pore (mPTP) inhibitor bongkreik acid (BKA) mimics the short-term potentiation (STP) and calcium transient phenotypes of *Df(16)5*^{+/-} and *Mrpl40*^{+/-} mice. (a–f) BKA effect on augmentation (a, d), peak GCaMP6 (b, e) and peak mitoGCaMP6 fluorescence intensities (c, f) in wild-type (WT) and *Df(16)5*^{+/-} littermates (a–c) or WT and *Mrpl40*^{+/-} littermates (normalized to WT levels) (d–f). Numbers of neurons or fluorescent puncta are shown inside columns. * $P < 0.05$.

(Figure 4a and Supplementary Figures S12b and d). BKA also did not affect basal synaptic transmission ($F_{(3,12)} = 1.179$, $P = 0.318$), paired-pulse facilitation ($F_{(3,5)} = 0.402$, $P = 0.752$) or recovery from depression ($F_{(3,23)} = 1.114$, $P = 0.358$) in either WT or *Df(16)5*^{+/-} mice (Supplementary Figure S13), indicating that the BKA effect is specific for the augmentation component of STP. Furthermore, BKA significantly enhanced the magnitudes of cytosolic and mitochondrial Ca²⁺ transients evoked by the 80-Hz train in WT mice (GCaMP6: $Q = 2.821$, $P < 0.05$; mitoGCaMP6: $Q = 4.908$, $P < 0.05$) (Figures 4b and c and Supplementary Figures S12e and g) but failed to increase Ca²⁺ transients in *Df(16)5*^{+/-} mice (GCaMP6: $Q = 0.246$, $P > 0.05$; mitoGCaMP6: $Q = 1.767$, $P > 0.05$) (Figures 4b and c and Supplementary Figures S12f and h), suggesting that the STP enhancement in *Df(16)5*^{+/-} mutants acts through the same mechanisms as BKA.

Like *Df(16)5*^{+/-} mice, *Mrpl40*^{+/-} mice showed no effect of BKA on STP, augmentation or Ca²⁺ transients (STP: $U = 52$, $P = 0.371$; augmentation: $t_{(23)} = -1.091$, $P = 0.287$; GCaMP6: $Q = 0.418$, $P > 0.05$; mitoGCaMP6: $Q = 0.052$, $P > 0.05$) in presynaptic terminals or mitochondria, whereas BKA enhanced these parameters in WT littermates (STP: $t_{(13)} = -3.685$, $P = 0.0028$; augmentation: $t_{(13)} = -0.2670$, $P = 0.02$; GCaMP6: $Q = 5.038$, $P < 0.05$; mitoGCaMP6: $Q = 2.645$, $P < 0.05$) (Figures 4d–f and Supplementary Figure S14). These results suggest that haploinsufficiency of the *Df(16)5* gene *Mrpl40* impairs Ca²⁺ handling by mPTP. Therefore, we sought to rescue this deficit by enhancing mPTP function through over-expression of ANTs. To that end, we designed the AAV-*Slc25a4* OE (Figure 5), which overexpresses *Ant1* (also known as *Slc25a4*), a gene encoding a regulator of mPTP activity.^{40,41} Only three isoforms of *Ant* (*Ant1*, 2 and 4) have been found in mice,^{42,43} and we identified *Ant1* as the highest expressed isoform in the mouse hippocampus (data not shown). When expressed in the hippocampus, AAV-*Slc25a4* OE increased the level of Slc25a4 protein ($t_{(7)} = 7.868$, $P < 0.001$) (Supplementary Figures S15a and b). We verified that AAV-*Slc25a4* OE did not change the localization of Slc25a4 protein to mitochondria. Thus, Slc25a4 was co-localized with the mitochondrial fluorescent marker mitotracker (Supplementary Figure S15c), and AAV-*Slc25a4* OE did not change this pattern (Supplementary Figure S15d). AAV-*Slc25a4* OE expressed in the CA3 area of the hippocampus (Figure 5a) rescued STP and augmentation in *Mrpl40*^{+/-} mice (STP: $U = 15$, $P = 0.005$; augmentation: $t_{(22)} = 2.543$, $P = 0.019$) but did not affect WT littermates (STP: $t_{(16)} = 0.566$, $P = 0.578$; augmentation: $t_{(16)} = -0.654$, $P = 0.522$) (Figure 5b and Supplementary Figure S16).

To confirm that the BKA-induced reduction in mPTP function mimics the *Df(16)5*^{+/-} phenotype, we downregulated Slc25a4 by using the shRNA approach. To that end, we injected lentiviruses encoding three different shRNAs against *Slc25a4* into the CA3 area of the hippocampus. STP and augmentation of synaptic transmission at CA3–CA1 synapses increased in WT mice infected with all three *Slc25a4* shRNAs compared with the control shRNA (shRNA1 STP: $t_{(13)} = -1.882$, $P = 0.041$; augmentation: $U = 9$, $P = 0.029$; shRNA2 STP: $t_{(15)} = -1.910$, $P = 0.04$; augmentation: $t_{(17)} = -2.757$, $P = 0.014$; shRNA3 STP: $U = 9$, $P = 0.02$; augmentation: $t_{(13)} = -2.475$, $P = 0.028$) (Figure 5c and Supplementary Figure S17). However, *Slc25a4* shRNAs did not further affect STP or augmentation in *Mrpl40*^{+/-} mice (shRNA1 STP: $U = 23$, $P = 0.382$; augmentation: $U = 28$, $P = 0.721$; shRNA2 STP: $U = 23$, $P = 0.091$; augmentation: $t_{(19)} = 1.038$, $P = 0.312$; shRNA3 STP: $U = 27$, $P = 0.267$; augmentation: $U = 24$, $P = 0.107$) (Figure 5c and Supplementary Figure S17), suggesting that *Mrpl40* haploinsufficiency altered STP by affecting mPTP function.

DISCUSSION

Approximately 30% of patients with 22q11DS meet the diagnostic criteria for SCZ.⁴ Cognitive symptoms of SCZ include deficits in

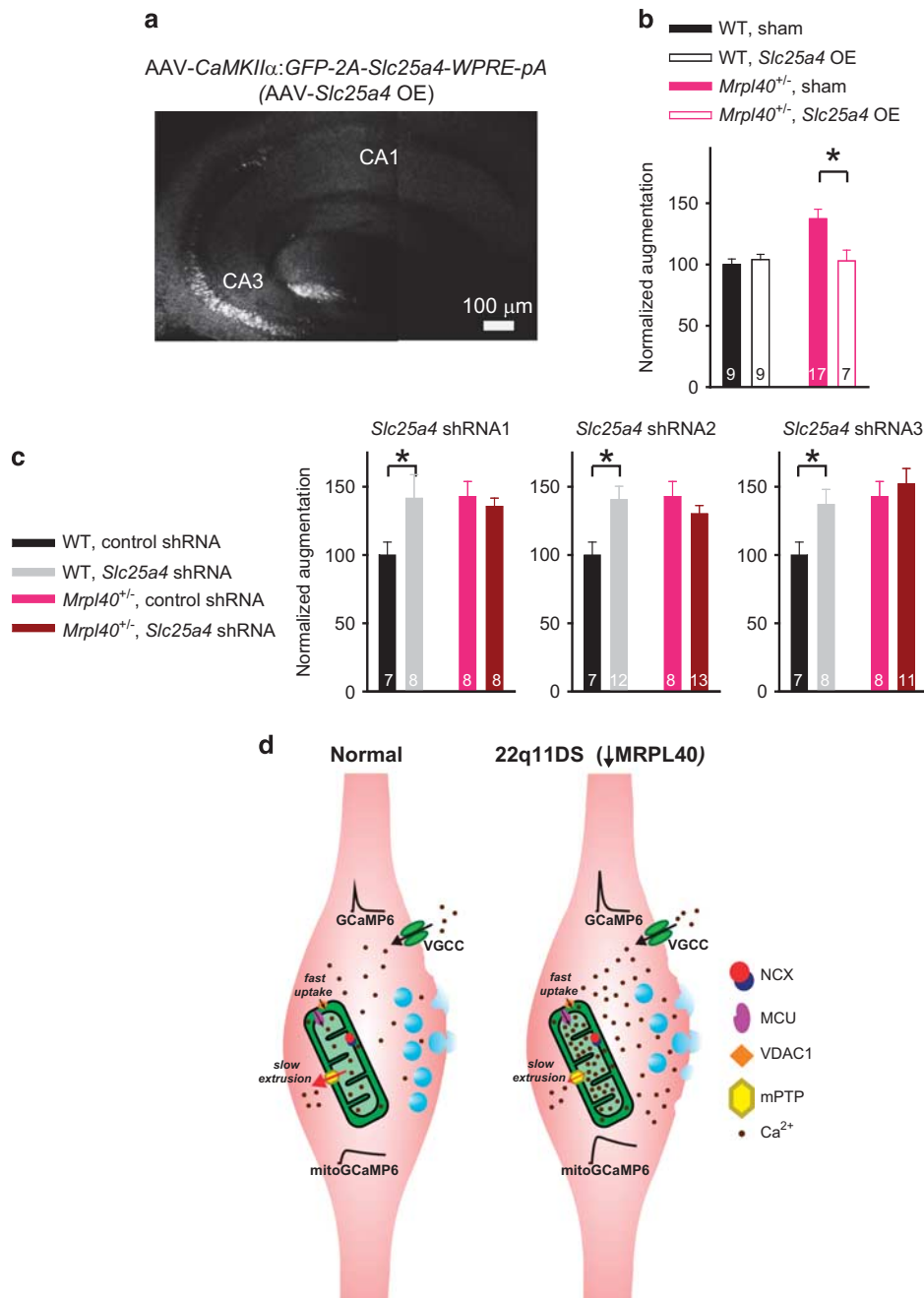


Figure 5. The mitochondrial permeability transition pore (mPTP) gain- or loss-of-function molecular manipulations rescue or mimic, respectively, the short-term potentiation (STP) phenotypes of *Mrpl40*^{+/-} mice. **(a)** Overexpression of *Slc25a4* and GFP in the CA3 area of the hippocampus. **(b)** Mean augmentation measured in sham- or *Slc25a4* OE-injected WT and *Mrpl40*^{+/-} mice. **(c)** Mean augmentation measured in control or *Slc25a4* shRNA-injected WT and *Mrpl40*^{+/-} mice. The data are shown for three different *Slc25a4* shRNAs (shRNA1, shRNA2, shRNA3) and are normalized to respective WT control levels. Numbers of neurons are shown inside columns. **P* < 0.05. **(d)** Model of mPTP-dependent mechanisms of STP dysfunction in 22q11DS. *MRPL40* haploinsufficiency in 22q11DS reduces mitochondrial Ca^{2+} extrusion through impaired mPTP. This leads to a Ca^{2+} build-up in the mitochondrial matrix and enhanced Ca^{2+} transients in the mitochondrial matrix and cytosol during high-frequency activity, which in turn leads to enhanced synaptic vesicle release in presynaptic terminals. MCU, mitochondrial Ca^{2+} uniporter; NCX, $\text{Na}^+/\text{Ca}^{2+}$ exchanger; VDAC1, voltage-dependent anion channel 1; VGCC, voltage-gated calcium channels; WT, wild type. Upper traces represent cytosolic Ca^{2+} transients (GCaMP6), and lower traces represent mitochondrial Ca^{2+} transients (mitoGCaMP6).

working memory, attention, executive function, and learning and memory; these symptoms have a more prognostic value than do the positive or negative symptoms of the disease, and they contribute more to the patients' functional disability.⁴⁴ The mechanisms underlying the cognitive deficits in SCZ and 22q11DS are still debated. Here we presented evidence that 22q11DS affects working memory and STP through a novel

pathogenic mechanism—abnormal Ca^{2+} handling by mitochondria. We also elucidated several features of this pathogenic mechanism: (1) By screening mice carrying hemizygous deletions of individual genes mapped within the distal part of the 22q11 microdeletion, we identified *Mrpl40* as a culprit gene that causes abnormal STP. (2) We identified that the augmentation component of STP is specifically affected. (3) *Mrpl40* haploinsufficiency

led to abnormal STP through mitochondria-mediated deregulation of presynaptic Ca^{2+} levels. (4) We pinpointed a functional abnormality in mitochondrial Ca^{2+} extrusion through the mPTP as a pathogenic mechanism caused by *Mrpl40* haploinsufficiency. (5) *Mrpl40* haploinsufficiency led to deficits in working memory but not in long-term plasticity or long-term memory.

The hippocampus, prefrontal cortex and interactions between these brain regions all contribute to working memory.^{45–48} Deficits in working memory in patients with SCZ and/or 22q11DS are well documented.^{49,50} STP, an associative, short-lived synaptic strengthening, is considered a cellular correlate of short-term memory, a term often used synonymously with working memory.^{20,51} Consistent with this notion, deficits in STP are well established in animal models of SCZ and 22q11DS.^{12,48,52–54}

Because symptoms of SCZ typically appear during late adolescence or early adulthood, age appears to be an important variable in synaptic plasticity phenotypes associated with 22q11DS mice. In our experiments, we used mice that were older than 4 months. At this age, STP and long-term potentiation at CA3–CA1 synapses are substantially increased in *Df(16)1^{+/-}* mouse models of 22q11DS, whereas at younger ages, both forms of synaptic plasticity are normal.²³ These experiments led to the identification of the microRNA-processing gene *Dgcr8* as the culprit gene residing in the proximal part of the microdeletion affecting both short- and long-term synaptic plasticity in the hippocampus. Deletion of one allele of *Dgcr8* causes depletion of *miR-185* and *miR-25* and post-transcriptional upregulation of *Serca2* in the forebrain of older but not younger mice.²³

Because 22q11DS is a multigene syndrome, it is extremely likely that more than one gene is involved in STP abnormalities. Our present work showed that deletion of one allele of *Mrpl40* residing in the distal part of the microdeletion, which is outside of the *Df(16)1* genomic region, caused *Dgcr8*-independent deficits in STP and working memory in 22q11DS. First, we identified the STP increase in *Df(16)5^{+/-}* mice, which were hemizygous for genes that mapped distally to *Dgcr8*. The STP screen revealed that only *Mrpl40^{+/-}* mice replicated the *Df(16)5^{+/-}* phenotype. Furthermore, the *Mrpl40*-related STP increase was mechanistically distinct from the STP increase identified in *Dgcr8^{+/-}* mice. *Dgcr8* haploinsufficiency elevates the *Serca2* protein,¹² but in the *Df(16)5^{+/-}* mice, *Serca2* levels were normal, and the *Serca* inhibitor thapsigargin did not rescue the STP defect.

Mrpl40 was originally identified as a nuclear gene involved in mitochondrial function.⁵⁵ Mitochondrial dysfunction has been strongly implicated in SCZ pathophysiology,⁵⁶ though the exact connection between SCZ pathogenesis and mitochondria has not been established. For instance, the gene encoding DISC1 (disrupted-in-schizophrenia 1) has been localized to mitochondria and is involved in maintaining mitochondrial morphology and regulating mitochondrial transport.⁵⁷ Several mitochondrial genes, including *Mrpl40*, are mapped within the 22q11.2 locus and expressed in the brain throughout development, thus implicating mitochondria in the pathogenesis of 22q11DS.^{58,59} *Mrpl40* haploinsufficiency does not affect the mitochondrial ultrastructure and does not reduce mitochondrial numbers in presynaptic terminals or total mitochondrial DNA, which is consistent with the view that SCZ is not a neurodegenerative disease. This is also consistent with our observations that *Df(16)5^{+/-}* or *Mrpl40^{+/-}* mice develop normally and have normal gross brain morphology.

Mitochondria provide energy through oxidative phosphorylation and regulate Ca^{2+} dynamics during synaptic transmission in neurons. Because of the mitochondrion's high capacity for Ca^{2+} uptake, it acts as a rapid buffering system during periods of intense synaptic activity, then slowly releases Ca^{2+} when activity subsides. This rapid uptake of Ca^{2+} into mitochondria occurs through channels (i.e., voltage-dependent anion channel VDAC1) in the outer membrane and the mitochondrial calcium uniporter in the inner membrane. Ca^{2+} is slowly released from the

mitochondria through the calcium exchangers and via the mPTP. mPTP has been shown to open during high-frequency stimulation in mammalian neurons, and that transient activation of the mPTP may play a role in the normal contribution of mitochondria to STP.⁶⁰

Oxidative phosphorylation appeared to be normal, whereas Ca^{2+} dynamics in presynaptic terminals was substantially altered in *Df(16)5^{+/-}* and *Mrpl40^{+/-}* mice. Our two-photon Ca^{2+} imaging in presynaptic terminals revealed that synaptic high-frequency stimulation that induces STP evokes enhanced Ca^{2+} transients in both the presynaptic mitochondrial matrix and presynaptic cytosol of mutant mice. These data argue for a problem with mitochondrial Ca^{2+} extrusion rather than with mitochondrial Ca^{2+} uptake. Indeed, if *Mrpl40* haploinsufficiency reduced the Ca^{2+} uptake into mitochondria, we would expect to see increased amplitudes of cytoplasmic Ca^{2+} transients but decreased Ca^{2+} transients within mitochondria. Our data are more consistent with a model for a reduced Ca^{2+} extrusion from mitochondria. Impaired Ca^{2+} extrusion from mitochondria will result in Ca^{2+} accumulation in the mitochondrial matrix, and this will contribute to the fast rise in mitochondrial Ca^{2+} that we observed with mitoGCaMP6. This will then reduce the effective mitochondrial buffering capacity and lead to enhanced cytoplasmic Ca^{2+} transients that we observed with the cytoplasmic GCaMP6 (Figure 5d). Moreover, slow Ca^{2+} extrusion from mitochondria (evident from extremely slow decay times of mitoGCaMP6) is an unlikely contributor to fast cytosol Ca^{2+} transients that occur during high-frequency synaptic activity.

Because inhibition of mPTP but not the mitochondrial $\text{Na}^{+}\text{-Ca}^{2+}$ exchanger increased presynaptic Ca^{2+} transients in WT mice, we concluded that the main route of Ca^{2+} extrusion from mitochondria during STP is mPTP. In WT mice, the pharmacological or molecular inhibition of mPTP with BKA or *Slc25a4* shRNA, respectively, mimicked the STP and Ca^{2+} -transient phenotypes we observed in *Df(16)5^{+/-}* and *Mrpl40^{+/-}* mice. Moreover, AAV-*Slc25a4* OE rescued the STP abnormality in *Mrpl40^{+/-}* mice, indicating that deletion of one allele of *Mrpl40* causes mPTP deficiency and STP increase.

Although our experiments demonstrated that *Mrpl40* haploinsufficiency leads to abnormal Ca^{2+} handling by mitochondria during STP, the exact connection between *Mrpl40* and mPTP function remains unclear. Some pharmacological agents that affect mPTP function⁶¹ can be beneficial adjuvants to antipsychotics to alleviate SCZ symptoms.⁵⁶ However, because mPTP is involved not only in Ca^{2+} extrusion from mitochondria but also in ATP transport, we cannot rule out the possibility that impaired mPTP regulation leads to the abnormal production of ATP in presynaptic terminals, which in turn could result in abnormal presynaptic function. This theory could be addressed using a novel ATP probe that visualizes ATP dynamics in the presynaptic terminals of neurons in culture, but those experiments have not yet been tailored for acute brain slices.⁶²

In summary, we report that haploinsufficiency of *Mrpl40*, a gene mapped within the 22q11.2 microdeletion associated with SCZ, causes deficient working memory. This behavioral abnormality, which typically manifests in patients with SCZ, is associated with abnormal STP changes in synaptic transmission in the hippocampus and caused by elevated presynaptic Ca^{2+} and impaired Ca^{2+} extrusion from mitochondria.

CONFLICT OF INTEREST

The authors declare no conflict of interest.

ACKNOWLEDGMENTS

This work was supported, in part, by National Institutes of Health grants R01 MH095810 and R01 MH097742, NARSAD Independent Investigator Grant, and by ALSAC (SSZ). We thank Drs Elizabeth Illingworth, Peter Scambler and Mikio Furuse for

providing *Df(16)5^{+/-}*, *Hira^{+/-}* and *Cldn5^{+/-}* mice; Sharon Frase, Randall Wakefield and staff in the Electron Microscopy Division of the St. Jude Cell and Tissue Imaging Center for help with electron microscopy; John Swift, Amber Braden, Lisa Emmons and staff in the St. Jude Transgenic Core for help in producing mouse mutants; and staff in the St. Jude and University of Tennessee Vector Cores for producing the AAVs and lentiviruses. We also thank Jay Blundon for valuable comments and Angela McArthur and Vani Shanker for editing the manuscript.

REFERENCES

- Carpenter WT Jr, Buchanan RW. Schizophrenia. *N Engl J Med* 1994; **330**: 681–690.
- Nestler EJ, Hyman SE. Animal models of neuropsychiatric disorders. *Nat Neurosci* 2010; **13**: 1161–1169.
- Scambler PJ. The 22q11 deletion syndromes. *Hum Mol Genet* 2000; **9**: 2421–2426.
- Pulver AE, Nestadt G, Goldberg R, Shprintzen RJ, Lamacz M, Wolyniec PS et al. Psychotic illness in patients diagnosed with velo-cardio-facial syndrome and their relatives. *J Nerv Ment Dis* 1994; **182**: 476–478.
- Chow EW, Watson M, Young DA, Bassett AS. Neurocognitive profile in 22q11 deletion syndrome and schizophrenia. *Schizophr Res* 2006; **87**: 270–278.
- Lewis DA. Cortical circuit dysfunction and cognitive deficits in schizophrenia—implications for preemptive interventions. *Eur J Neurosci* 2012; **35**: 1871–1878.
- Vorstman JA, Breetvelt EJ, Duijff SN, Eliez S, Schneider M, Jalbrzikowski M et al. Cognitive decline preceding the onset of psychosis in patients with 22q11.2 deletion syndrome. *JAMA Psychiatry* 2015; **72**: 377–385.
- Heckers S, Rauch SL, Goff D, Savage CR, Schacter DL, Fischman AJ et al. Impaired recruitment of the hippocampus during conscious recollection in schizophrenia. *Nat Neurosci* 1998; **1**: 318–323.
- Tamminga CA, Stan AD, Wagner AD. The hippocampal formation in schizophrenia. *Am J Psychiatry* 2010; **167**: 1178–1193.
- Kates WR, Krauss BR, Abdulsabur N, Colgan D, Antshel KM, Higgins AM et al. The neural correlates of non-spatial working memory in velocardiofacial syndrome (22q11.2 deletion syndrome). *Neuropsychologia* 2007; **45**: 2863–2873.
- Sobin C, Kiley-Brabeck K, Daniels S, Blundell M, Anyane-Yeboah K, Karayiorgou M et al. Networks of attention in children with the 22q11 deletion syndrome. *Dev Neuropsychol* 2004; **26**: 611–626.
- Earls LR, Bayazitov IT, Fricke RG, Berry RB, Illingworth E, Mittleman G et al. Dysregulation of presynaptic calcium and synaptic plasticity in a mouse model of 22q11 deletion syndrome. *J Neurosci* 2010; **30**: 15843–15855.
- Stark KL, Xu B, Bagchi A, Lai WS, Liu H, Hsu R et al. Altered brain microRNA biogenesis contributes to phenotypic deficits in a 22q11-deletion mouse model. *Nat Genet* 2008; **40**: 751–760.
- Kandaswamy U, Deng PY, Stevens CF, Klyachko VA. The role of presynaptic dynamics in processing of natural spike trains in hippocampal synapses. *J Neurosci* 2010; **30**: 15904–15914.
- Abbott LF, Regehr WG. Synaptic computation. *Nature* 2004; **431**: 796–803.
- Klyachko VA, Stevens CF. Excitatory and feed-forward inhibitory hippocampal synapses work synergistically as an adaptive filter of natural spike trains. *PLoS Biol* 2006; **4**: e207.
- Rotman Z, Deng PY, Klyachko VA. Short-term plasticity optimizes synaptic information transmission. *J Neurosci* 2011; **31**: 14800–14809.
- Mongillo G, Barak O, Tsodyks M. Synaptic theory of working memory. *Science* 2008; **319**: 1543–1546.
- Deco G, Rolls ET, Romo R. Synaptic dynamics and decision making. *Proc Natl Acad Sci USA* 2010; **107**: 7545–7549.
- Zucker RS, Regehr WG. Short-term synaptic plasticity. *Annu Rev Physiol* 2002; **64**: 355–405.
- Deng PY, Sojka D, Klyachko VA. Abnormal presynaptic short-term plasticity and information processing in a mouse model of fragile X syndrome. *J Neurosci* 2011; **31**: 10971–10982.
- Tu H, Nelson O, Bezprozvanny A, Wang Z, Lee SF, Hao YH et al. Presenilins form ER Ca²⁺ leak channels, a function disrupted by familial Alzheimer's disease-linked mutations. *Cell* 2006; **126**: 981–993.
- Earls LR, Fricke RG, Yu J, Berry RB, Baldwin LT, Zakharenko SS et al. Age-dependent microRNA control of synaptic plasticity in 22q11 deletion syndrome and schizophrenia. *J Neurosci* 2012; **32**: 14132–14144.
- Schizophrenia Working Group of the Psychiatric Genomics Consortium. Biological insights from 108 schizophrenia-associated genetic loci. *Nature* 2014; **511**: 421–427.
- Chen TW, Wardill TJ, Sun Y, Pulver SR, Renninger SL, Baohan A et al. Ultrasensitive fluorescent proteins for imaging neuronal activity. *Nature* 2013; **499**: 295–300.
- Lindsay EA, Vitelli F, Su H, Morishima M, Huynh T, Pramparo T et al. Tbx1 haploinsufficiency in the DiGeorge syndrome region causes aortic arch defects in mice. *Nature* 2001; **410**: 97–101.
- Nitta T, Hata M, Gotoh S, Seo Y, Sasaki H, Hashimoto N et al. Size-selective loosening of the blood-brain barrier in claudin-5-deficient mice. *J Cell Biol* 2003; **161**: 653–660.
- Roberts C, Sutherland HF, Farmer H, Kimber W, Halford S, Carey A et al. Targeted mutagenesis of the Hira gene results in gastrulation defects and patterning abnormalities of mesoendodermal derivatives prior to early embryonic lethality. *Mol Cell Biol* 2002; **22**: 2318–2328.
- Klyachko VA, Stevens CF. Temperature-dependent shift of balance among the components of short-term plasticity in hippocampal synapses. *J Neurosci* 2006; **26**: 6945–6957.
- Christensen M, Larsen LA, Kauppinen S, Schrott G. Recombinant adeno-associated virus-mediated microRNA delivery into the postnatal mouse brain reveals a role for miR-134 in dendritogenesis in vivo. *Front Neural Circuits* 2010; **3**: 16.
- Chun S, Westmoreland JJ, Bayazitov IT, Eddins D, Pani AK, Smeyne RJ et al. Specific disruption of thalamic inputs to the auditory cortex in schizophrenia models. *Science* 2014; **344**: 1178–1182.
- Denk W, Horstmann H. Serial block-face scanning electron microscopy to reconstruct three-dimensional tissue nanostructure. *PLoS Biol* 2004; **2**: e329.
- Paylor R, Glaser B, Mupo A, Ataliotis P, Spencer C, Sobotka A et al. Tbx1 haploinsufficiency is linked to behavioral disorders in mice and humans: implications for 22q11 deletion syndrome. *Proc Natl Acad Sci USA* 2006; **103**: 7729–7734.
- Greber BJ, Boehringer D, Leibundgut M, Bieri P, Leitner A, Schmitz N et al. The complete structure of the large subunit of the mammalian mitochondrial ribosome. *Nature* 2014; **515**: 283–286.
- Greber BJ, Boehringer D, Leitner A, Bieri P, Voigts-Hoffmann F, Erzberger JP et al. Architecture of the large subunit of the mammalian mitochondrial ribosome. *Nature* 2014; **505**: 515–519.
- Tang Y, Zucker RS. Mitochondrial involvement in post-tetanic potentiation of synaptic transmission. *Neuron* 1997; **18**: 483–491.
- Bernardi P, von SS. The permeability transition pore as a Ca(2+) release channel: new answers to an old question. *Cell Calcium* 2012; **52**: 22–27.
- Rizzuto R, De SD, Raffaello A, Mammucari C. Mitochondria as sensors and regulators of calcium signalling. *Nat Rev Mol Cell Biol* 2012; **13**: 566–578.
- Halestrap AP. What is the mitochondrial permeability transition pore? *J Mol Cell Cardiol* 2009; **46**: 821–831.
- Kokoszka JE, Waymire KG, Levy SE, Sligh JE, Cai J, Jones DP et al. The ADP/ATP translocator is not essential for the mitochondrial permeability transition pore. *Nature* 2004; **427**: 461–465.
- Bonora M, Pinton P. The mitochondrial permeability transition pore and cancer: molecular mechanisms involved in cell death. *Front Oncol* 2014; **4**: 302.
- Brower JV, Rodic N, Seki T, Jorgensen M, Fliess N, Yachnis AT et al. Evolutionarily conserved mammalian adenine nucleotide translocase 4 is essential for spermatogenesis. *J Biol Chem* 2007; **282**: 29658–29666.
- Levy SE, Chen YS, Graham BH, Wallace DC. Expression and sequence analysis of the mouse adenine nucleotide translocase 1 and 2 genes. *Gene* 2000; **254**: 57–66.
- Carter CS, Barch DM, Buchanan RW, Bullmore E, Krystal JH, Cohen J et al. Identifying cognitive mechanisms targeted for treatment development in schizophrenia: an overview of the first meeting of the Cognitive Neuroscience Treatment Research to Improve Cognition in Schizophrenia Initiative. *Biol Psychiatry* 2008; **64**: 4–10.
- Goldman-Rakic PS. Architecture of the prefrontal cortex and the central executive. *Ann NY Acad Sci* 1995; **769**: 71–83.
- Sanderson DJ, Good MA, Seeburg PH, Sprengel R, Rawlins JN, Bannerman DM et al. The role of the GluR-A (GluR1) AMPA receptor subunit in learning and memory. *Prog Brain Res* 2008; **169**: 159–178.
- Floresco SB, Seamans JK, Phillips AG. Selective roles for hippocampal, prefrontal cortical, and ventral striatal circuits in radial-arm maze tasks with or without a delay. *J Neurosci* 1997; **17**: 1880–1890.
- Sigurdsson T, Stark KL, Karayiorgou M, Gogos JA, Gordon JA. Impaired hippocampal-prefrontal synchrony in a genetic mouse model of schizophrenia. *Nature* 2010; **464**: 763–767.
- Wong LM, Riggins T, Harvey D, Cabral M, Simon TJ. Children with chromosome 22q11.2 deletion syndrome exhibit impaired spatial working memory. *Am J Intellect Dev Disabil* 2014; **119**: 115–132.
- Bearden CE, Woodin MF, Wang PP, Moss E, Donald-McGinn D, Zackai E et al. The neurocognitive phenotype of the 22q11.2 deletion syndrome: selective deficit in visual-spatial memory. *J Clin Exp Neuropsychol* 2001; **23**: 447–464.
- Lisman J. The challenge of understanding the brain: where we stand in 2015. *Neuron* 2015 **86**: 864–882.
- Crabtree GW, Gogos JA. Synaptic plasticity, neural circuits, and the emerging role of altered short-term information processing in schizophrenia. *Front Synaptic Neurosci* 2014; **6**: 28.
- Kvajo M, McKellar H, Arguello PA, Drew LJ, Moore H, MacDermott AB et al. A mutation in mouse *Disc1* that models a schizophrenia risk allele leads to specific alterations in neuronal architecture and cognition. *Proc Natl Acad Sci USA* 2008; **105**: 7076–7081.

- 54 Fenelon K, Mukai J, Xu B, Hsu PK, Drew LJ, Karayiorgou M *et al*. Deficiency of *Dgcr8*, a gene disrupted by the 22q11.2 microdeletion, results in altered short-term plasticity in the prefrontal cortex. *Proc Natl Acad Sci USA* 2011; **108**: 4447–4452.
- 55 Funke B, Puech A, Saint-Jore B, Pandita R, Skoultchi A, Morrow B *et al*. Isolation and characterization of a human gene containing a nuclear localization signal from the critical region for velo-cardio-facial syndrome on 22q11. *Genomics* 1998; **53**: 146–154.
- 56 Manji H, Kato T, Di Prospero NA, Ness S, Beal MF, Krams M *et al*. Impaired mitochondrial function in psychiatric disorders. *Nat Rev Neurosci* 2012; **13**: 293–307.
- 57 Atkin TA, MacAskill AF, Brandon NJ, Kittler JT. Disrupted in Schizophrenia-1 regulates intracellular trafficking of mitochondria in neurons. *Mol Psychiatry* 2011; **16**: 122–124, 121.
- 58 Napoli E, Tassone F, Wong S, Angkustsiri K, Simon TJ, Song G *et al*. Mitochondrial citrate transporter-dependent metabolic signature in the 22q11.2 deletion syndrome. *J Biol Chem* 2015; **290**: 23240–23253.
- 59 Maynard TM, Meechan DW, Dudevoir ML, Gopalakrishna D, Peters AZ, Heindel CC *et al*. Mitochondrial localization and function of a subset of 22q11 deletion syndrome candidate genes. *Mol Cell Neurosci* 2008; **39**: 439–451.
- 60 Barsukova A, Komarov A, Hajnoczky G, Bernardi P, Bourdette D, Forte M *et al*. Activation of the mitochondrial permeability transition pore modulates Ca²⁺ responses to physiological stimuli in adult neurons. *Eur J Neurosci* 2011; **33**: 831–842.
- 61 Gieseler A, Schultze AT, Kupsch K, Haroon MF, Wolf G, Siemen D *et al*. Inhibitory modulation of the mitochondrial permeability transition by minocycline. *Biochem Pharmacol* 2009; **77**: 888–896.
- 62 Rangaraju V, Calloway N, Ryan TA. Activity-driven local ATP synthesis is required for synaptic function. *Cell* 2014; **156**: 825–835.



This work is licensed under a Creative Commons Attribution-NonCommercial-NoDerivs 4.0 International License. The images or other third party material in this article are included in the article's Creative Commons license, unless indicated otherwise in the credit line; if the material is not included under the Creative Commons license, users will need to obtain permission from the license holder to reproduce the material. To view a copy of this license, visit <http://creativecommons.org/licenses/by-nc-nd/4.0/>

© The Author(s) (2017)

Supplementary Information accompanies the paper on the Molecular Psychiatry website (<http://www.nature.com/mp>)